FEDERAL UNIVERSITY OF PERNAMBUCO

TECHNOLOGY AND GEOCIENCES CENTER

MECHANICAL ENGINEERING DEPARTMENT

MECHANICAL ENGINEERING GRADUATE PROGRAM

TÚLIO DE MOURA CAVALCANTE

A FINITE VOLUME SCHEME COUPLED WITH A HYBRID-GRID METHOD FOR THE 2-D SIMULATION OF TWO-PHASE FLOWS IN NATURALLY FRACTURED RESERVOIRS

Recife

2019

TÚLIO DE MOURA CAVALCANTE

A FINITE VOLUME SCHEME COUPLED WITH A HYBRID-GRID METHOD FOR THE 2-D SIMULATION OF TWO-PHASE FLOWS IN NATURALLY FRACTURED RESERVOIRS

Thesis submitted to the faculty of the Mechanical Engineering Graduate Program of the Federal University of Pernambuco, as part of the requirements necessary to obtain a Master's degree in Mechanical Engineering.

Area of Concentration: Thermal Processes and Systems.

Surpervisor: Paulo Roberto Maciel Lyra, PhD.

Co-surpervisor: Darlan Karlo Elisiário de Carvalho, PhD.

Recife

2019

Catalogação na fonte
Bibliotecária Valdicéa Alves, CRB-4 / 1260

C376f Cavalcante, Túlio de Moura.
A finite volume scheme coupled with a hybrid-grid method for the 2-d simulation of two-phase flows in naturally fractured reservoirs - 2019.
81folhas, Il.; Tabs. Abr. e Simb.

Orientador: Prof. Dr. Paulo Roberto Maciel Lyra.
Coorientador: Prof. Dr. Darlan Karlo Elisiário de Carvalho.

Dissertação (Mestrado) – Universidade Federal de Pernambuco. CTG. Programa de Pós-Graduação em Engenharia Mecânica, 2019.
Inclui Referências e Apêndice.

Idioma Inglês.

1. Engenharia Mecânica. 2. Escoamento bifásico de óleo e água. 3. Reservatórios heterogêneos e anisotrópicos. 4. Reservatórios naturalmente fraturados. 5. Modelo de malha híbrida. 6. MPFA-D. I. Lyra, Paulo Roberto Maciel (Orientador). II. Carvalho, Darlan Karlo Elisiário de (Coordenador). III. Título.

UFPE

621 CDD (22. ed.) BCTG/2019-19

TÚLIO DE MOURA CAVALCANTE

A FINITE VOLUME SCHEME COUPLED WITH A HYBRID-GRID METHOD FOR THE 2-D SIMULATION OF TWO-PHASE FLOWS IN NATURALLY FRACTURED RESERVOIRS

Dissertação apresentada ao Programa de Pós-Graduação em Engenharia Mecânica do Departamento de Engenharia Mecânica, Centro de Tecnologia e Geociências da Universidade Federal de Pernambuco, como parte dos requisitos parciais para obtenção do título de mestre em Engenharia Mecânica

Aprovada em: 18/01/2019

BANCA EXAMINADORA

Prof. Dr. Paulo Roberto Maciel Lyra (Orientador)

Universidade Federal de Pernambuco

Prof. Dr. Darlan Karlo Elisiário de Carvalho (Coorientador)

Universidade Federal de Pernambuco

Prof. Dr. Ramiro Brito Willmersdorf (Examinador Externo)

Universidade Federal de Pernambuco

Prof. Dr. Márcio Rodrigo de Araújo Souza (Examinador Externo)

Universidade Federal da Paraíba

To the memory of my grandfather José.

À memória do meu avô José.

ACKNOWLEDGEMENTS

I thank God for good health, for bringing light to my mind and giving me those ideas that, if not the best, are the ones that always work.

I thank Geraldo, Ângela and Douglas, my family, for supporting me in every way and staying by my side in my successes or mistakes.

I thank my beloved Thayane for being my strength, no matter the circumstances.

I thank Professors Paulo Lyra and Darlan for the orientation and hours of conversation, helping me to fill in the blanks of my ideas.

I thank Professors Ramiro and Márcio for the attention dedicated to improving this text.

I thank all the colleagues of PADMEC for sharing their knowledges with me, especially Braian for his database and Fernando for our code.

I thank FACEPE for funding this work.

Agradeço a Deus pela saúde, por iluminar minha mente e me dar aquelas ideias que, se não as melhores, são as que sempre funcionam.

Agradeço a Geraldo, Ângela e Douglas, minha família, por me apoiarem em todos os sentidos e ficarem ao meu lado em meus acertos ou erros.

Agradeço à minha amada Thayane por ser minha força, não importando as circunstâncias.

Agradeço aos Professores Paulo Lyra e Darlan pela orientação e pelas horas de conversa que me ajudaram a preencher as lacunas das minhas ideias.

Agradeço aos Professores Ramiro e Márcio pela atenção dedicada à melhoria deste texto.

Agradeço a todos os colegas do PADMEC por compartilharem seus conhecimentos comigo, especialmente a Braian por seu banco de dados e a Fernando pelo nosso código.

Agradeço à FACEPE por financiar este trabalho.

ABSTRACT

Two-phase flows of oil and water in naturally fractured petroleum reservoirs can be described by a system of nonlinear partial differential equations that comprises an elliptic pressure equation and a hyperbolic saturation equation coupled through the total velocity field. Modeling this problem is a great challenge, due to the complexity of the depositional environments, which can include fractures (channels or barriers). In such cases, it is particularly complex to construct structured meshes which are capable of properly modeling the reservoir. In this work, a locally conservative approach to model the oil and water displacements in naturally fractured reservoirs using general unstructured meshes was developed. A cell-centered Finite-Volume Method with a Multi-Point Flux Approximation that uses the so called "diamond stencil" (MPFA-D) was used to solve the pressure equation, coupled with a Hybrid-Grid Method (HyG) to deal with the fractures. The classical First Order Upwind Method (FOUM) was used to solve the saturation equation. The FOUM was applied in two different segregated schemes, in its explicit and implicit versions, respectively the IMPES (IMplicit Pressure and Explicit Saturation) and the SEQ (SEQuential implicit pressure and saturation). The MPFA-D is a very robust and flexible formulation that is capable of handling highly heterogeneous and anisotropic domains using general polygonal meshes. In the HyG, the mesh that discretizes the domain must fit the spatial positions of the fractures, so that they are associated to edges - as 1-D cells in a 2-D mesh -, therefore, the calculation of the fluxes in these edges is dependent on the pressures on fractures and on the adjacent volumes, but, in this strategy, the fractures are expanded, in the computational domain, to the same dimension of the mesh. In this way, it is possible to get, for example, 2-D fracture cells in a 2-D mesh, but avoiding excessive refinement in the fractured regions, in the original mesh. The proposed formulation presented quite remarkable results when compared with similar formulations using classical full pressure support and triangle pressure support methods, or even the with MPFA-D itself when using an equidimensional approach.

Keywords: Two-phase flows of oil and water. Heterogeneous and anisotropic reservoirs. Naturally fractured reservoirs. Hybrid-grid method. MPFA-D.

RESUMO

Escoamentos bifásicos de óleo e água em reservatórios de petróleo naturalmente fraturados podem ser descritos por um sistema de equações diferenciais parciais não-lineares que compreende uma equação elíptica de pressão e uma equação hiperbólica de saturação acopladas através do campo de velocidade total. Modelar este tipo de problema é um grande desafio, devido à complexidade dos ambientes deposicionais, que pode incluir fraturas (canais ou barreiras). Em tais casos, é particularmente complexo construir malhas estruturadas capazes de modelar adequadamente o reservatório. Neste trabalho, foi desenvolvida uma formulação localmente conservativa para modelar os escoamentos de óleo e água em reservatórios naturalmente fraturados usando malhas não-estruturadas. Para resolver a equação da pressão, foi adaptado um método de volumes finitos centrado na célula com uma aproximação de fluxo por múltiplos pontos que usa o chamado "estêncil de diamante" (MPFA-D) acoplado a um método de malha híbrida (HyG) para lidar com as fraturas. O clássico método de ponderação à montante de primeira ordem (FOUM) foi usado para resolver a equação de saturação. O FOUM foi aplicado em dois esquemas segregados diferentes, em suas versões explícita e implícita, respectivamente o IMPES (solução IMplícita para a Pressão e Explícita para a Saturação) e o SEQ (solução SEQuencialmente implícita para pressão e saturação). O MPFA-D é uma formulação muito robusta e flexível que é capaz de lidar com domínios altamente heterogêneos e anisotrópicos usando malhas poligonais quaisquer. No HyG, a malha que discretiza o domínio deve ajustar-se às posições espaciais das fraturas, de forma que elas estejam associadas a arestas - como células 1-D em uma malha 2-D -, portanto, o cálculo dos fluxos nessas arestas é dependente das pressões nas fraturas e nos volumes adjacentes, mas, nessa estratégia, as fraturas são expandidas, no domínio computacional, para a mesma dimensão da malha. Dessa forma, é possível obter, por exemplo, células de fratura 2-D em uma malha 2-D, mas evitando-se refinamentos excessivos nas regiões das fraturas, na malha original. A formulação proposta apresentou bons resultados quando comparada com formulações similares utilizando métodos clássicos com suporte total e suporte triangular para a pressão, ou mesmo com o próprio MPFA-D, numa abordagem equidimensional.

Palavras-chave: Escoamento bifásico de óleo e água. Reservatórios heterogêneos e anisotrópicos. Reservatórios naturalmente fraturados. Modelo de malha híbrida. MPFA-D.

LIST OF FIGURES

LIST OF TABLES

LIST OF ABBREVIATIONS AND ACRONYMS

LDFM	Lower-Dimensional Fracture Model
HyG	Hybrid-Grid Method
CVFD	Control Volume Finite Difference Method
TPFA	Two-Point Flux Approximation
MPFA	Multipoint Flux Approximation
MPFA-O	Multipoint Flux Approximation Variant with “O” Stencil
MPFA-FPS	Multipoint Flux Approximation Variant with Full Pressure Support
MPFA-D	Multipoint Flux Approximation Variant with “Diamond” Stencil
FOUM	First Order Upwind Method
IMPES	Implicit Pressure and Explicit Saturation Scheme
SEQ	Sequential Implicit Scheme
2-D	Two Dimensions
3-D	Three Dimensions
LPEW2	Linearity Preserving Explicit Weighting type 2
PADMEC	Researching Group on High-Performance Processing in Computational Mechanics
UFPE	Federal University of Pernambuco
CV	Control Volume
CFL	Courant–Friedrichs–Lewy Condition
CVD-MPFA	Control Volume Distributed Variant of Multipoint Flux Approximation
FPS	Full-Pressure Support
TPS	Triangle Pressure Support
PVI	Porous Volume Injected

CONTENTS

1 INTRODUCTION

Most of physical phenomena observed in nature that are relevant to mankind are described through mathematical models, so that they can be used to perform simulations, i.e., predictions of results associated with those physical phenomena. In this context, one of the phenomena of interest is the flow of fluids in porous media, whose mathematical model comes from the experiments of Henry Darcy, in a hospital in Dijon, France, in 1856. This phenomenon is intrinsically associated with the production of petroleum, a process that involves the displacement of hydrocarbons through a porous reservoir and whose importance to the global economy is fundamental. Its simulation represents a very important tool in order to obtain information that allows an adequate management of the production, aiming at optimizing the recovery of hydrocarbons and maximizing the economic return of the process (CHEN; HUAN; MA, 2006; EWING, 1983; PEACEMAN, 1977).

Oil recovery generally takes place initially with the drilling of wells, which functions as outlets for oil stored at high pressures in the reservoir. This process is called primary recovery. When the reservoir pressure is not enough to expel the oil, the drilling of injection wells is required, through which fluids are injected to increase the pressure in the reservoir and make feasible the oil recovery. This process is called secondary recovery. In the case in which water is used as the injected fluid in the secondary recovery and it is assumed that the pressure of the reservoir does not fall sufficiently to lead to the appearance of a gas phase, the secondary recovery process can be simplified as a two-phase flow.

The two-phase flow in heterogeneous and anisotropic media, as petroleum reservoirs, after considering some simplifying hypotheses, can be described, as a system of nonlinear partial differential equations, composed by an elliptic pressure equation and a hyperbolic transport equation. The modeling of this problem is a great challenge, due to the complexity of depositional environments that typically includes inclined layers, faults and fractures (channels or barriers) with different sizes and shapes.

The fractures can be the result of external stresses during the production process or have origin in the geological activities during the formation of the reservoir system. This last type is what characterizes the naturally fractured reservoirs, which have received increasing attention, because the oil industry estimates that most of the remaining exploitable fields are of this type (MATTHÄI, 2005).

Sandve, Berre and Nordbotten (2012) terms as fractures all the reservoirs systems of discontinuities and affirm that they can occur on different scales, with different geometries, and may behave as either channels or barriers for the fluid flow. Martin, Jaffré and Roberts (2005) affirm that the case in which there is a small permeability in the fracture involves a pressure discontinuity and the case in which there is a large permeability in the fracture involves a velocity discontinuity.

Since the mid-20th century, different strategies have been studied to deal with fractured reservoirs. The most intuitive of all is single-continuum approach, which consists of upscaling the properties over the fractured regions to obtain equivalent properties (i.e., porosity, permeability, etc.), but the presence of the fractures within the porous media frequently introduce strong discontinuities that are not well represented by averaged descriptions (LONG et al., 1982). Therefore, since the beginning of the studies of the infiltration in fractured media, it was sought to build a multi-continuum approach, in which no geometric distinctions would be made between matrix and fractures, but instead employ different media that coexist in space, with transfer functions relating them (BERRE; DOSTER; KEILEGAVLEN, 2018).

Barenblatt, Zheltov and Kochina (1960) considered that a fractured (what they called fissured) rock consisted of pores and permeable blocks separated one from each other by a system of fractures, whose widths are considerably greater than the characteristic dimensions of the pores, what makes the permeability of the fracture system considerably bigger than permeability of the blocks pores system. On the other hand, the total volume of the fractures is much smaller than the total porous volume, so that the ratio between the total fractures volume and the rock volume is considerably smaller than the porosity of the blocks. From this model, the first and most commonly used approach to treat naturally fractured domains was developed, which uses effective parameters to derive the behavior of the fluid in a dual-continuum context (BARENBLATT; ZHELTOV; KOCHINA, 1960; WARREN; ROOT, 1963). This family of strategies has been called dual-porosity models, in which the reservoir is modelled as a highly interconnected and structured set of fractures supplied by fluids from numerous small matrix blocks (ULEBERG; KLEPPE, 1996). For two-phase flow, the dual-continuum methods need a very complex basis, in terms of constitutive relations for capillary pressures and relative permeabilities, and transfer functions, to ensure an accurate solution (HOTEIT; FIROOZABADI, 2008; BERRE; DOSTER; KEILEGAVLEN, 2018).

Other conventional way to incorporate the effects of the fractures in a flow simulator is using transmissibility multipliers that account for the reduced or increased permeability for each cross-fracture connection (MANZOCCHI et al., 1999; NILSEN et al., 2012). Transmissibility multipliers are typically calculated as empirical functions and are highly grid dependent and strictly associated with a connection between two grid cells rather than with the fracture itself. Therefore, if the grid is refined, the fractures permeabilities must be recalculated and then translated back to new multipliers values. Regarding the modelling, the transmissibility multipliers are not good solutions because any given multiplier value will be tied to a specific discretization and the introduction of these values into another consistent scheme will produce large pointwise errors (NILSEN et al., 2012).

On the other hand, some strategies which describe the fractures explicitly have also been developed. These methods are more suitable for multiphase flow problems, because, if the constitutive relations for capillary pressures and relative permeabilities are known, they can be included directly into the models (BERRE; DOSTER; KEILEGAVLEN, 2018). However, these strategies are frequently associated to matrix ill-conditioning and excessive time steps restrictions due to the geometrical scales contrast between the fracture and the rock matrix grid cells (GHORAYEB; FIROOZABADI, 2000).

The explicit fracture representation methods can be divided in two groups, based on the discretization approaches: the conforming mesh and the non-conforming mesh formulations. In the first one, the mesh construction needs to fit the fractures positions (this condition makes this strategy especially costly when it is necessary to discretize small angles and small distances), which is not needed in the second one, in which the fractures can cross through the rock matrix grid-cells. In this second group, there are the extended finite elements methods (FUMAGALLI; SCOTTI, 2013; SCHWENCK et al., 2015; FLEMISCH; FUMAGALLI; SCOTTI, 2016), which are applicable only for finite elements methods, and the embedded discrete fracture models (LI; LEE, 2008), in which the degrees of freedom of matrix and fractures are discretized separately, but the coupling structure is identical to that of dual-continuum, with the difference that the coupling terms is modeled in terms of discrete variables directly (BERRE; DOSTER; KEILEGAVLEN, 2018).

The mesh conforming methods can also be subdivided in three groups: the equidimensional strategy, the lower-dimensional fracture models and the hybrid-grid methods. The equidimensional strategy is certainly the costliest one, in which the fractures are treated as *n*-dimensional entities in a *n*-dimensional domain (2-D surfaces in a 2-D domain,

for example). In this case, they are represented in the geometric mesh with its real aperture and the inside of the fracture is discretized as the rest of the domain. On the other hand, the lower-dimensional - also called mixed-dimensional (BERRE; DOSTER; KEILEGAVLEN, 2018) - fracture models (MARTIN; JAFFRÉ; ROBERTS, 2005; HOTEIT; FIROOZABADI, 2008; AHMED et al., 2015) and the hybrid-grid methods (KARIMI-FARD; DURLOFSKY; AZIZ, 2004; SANDVE; BERRE; NORDBOTTEN, 2012; AHMED et al., 2017) describe the fractures explicitly as (n-1)-dimensional cells in a n-dimensional domain, for example as 1-D lines in 2-D surfaces (NOORISHAD; MEHRAN, 1982; BACA; ARNETT; LANGFORD, 1984; MARTIN; JAFFRÉ; ROBERTS, 2005), what improves considerably the computational efficiency (HOTEIT; FIROOZABADI, 2008). However, it is still not feasible to use them to treat domains with high quantity (thousands) of fractures, due to computational capacity limitations. In these cases, it is possible to use an upscaling technique to mimic the effect of most fractures, using those types of strategies just for the most relevant ones (LEE; LOUGH; JENSEN, 2001).

In the lower-dimensional fracture models (LDFM), the flow equations for the fractures are discretized separately from the matrix, in a (n-1)-dimensional subdomain. Otherwise, in the hybrid-grid methods (HyG), the fractures are expanded to n-dimensional in the computational domain, so the equations for the fractures and for the rock matrix are discretized together, which make them more adequate to take full advantage from full pressure support (FPS) methods when solving the pressure equation.

Thus, the hybrid-grid method meets the characteristics of capability to represent complex geometries and easiness to improve the representation of physics, despite the computational cost increasing, when compared to those methods which do not represent the fractures explicitly. It is also more capable of taking full advantage from full pressure support methods, when compared to the lower-dimensional model, and without an important increasing of computational cost.

The formulation that has been traditionally used to discretize the governing equations is the control volume finite difference (CVFD) method (PEACEMAN, 1977; AZIZ; SETTARI, 1979; ERTEKIN; ABOU-KASSEM; KING, 2001), also called Two-Point Flux Approximation (TPFA) method, due its simplicity as well as its robustness and its association with structured grids, what, in general, leads to low computational cost, besides being easy to implement (CARVALHO, 2005). On the other hand, there are difficulties in representing complex geometries with structured meshes, cases in which the use of an excessive number of

blocks, in order to reduce the errors, can make the problem overly computationally costly, besides this, the CVFD only guarantees the convergence if the case of K-orthogonality, i.e., when the permeability tensor principal directions is aligned with the mesh axes (SOUZA, 2015).

Whenever it is necessary to deal with a full permeability tensor or a non-orthogonal grid, a multipoint flux approximation (MPFA) is, in general, required. The MPFA stencil is constructed to enforce flux continuity at a point on the interface between neighboring blocks and essentially generalizes the harmonic permeability averages used in TPFA (HE; DURLOFSKY, 2006). This family of methods was developed simultaneously by Aavatsmark, Barkve and Mannseth (1998.a; 1998.b), who has given it this name (MPFA), and Edwards and Rogers (1998). Since the appearance of other variants of MPFA, this specific formulation presented by Aavatsmark, Barkve and Mannseth (1998.a, 1998.b), have been called MPFA-O, because of the format of the set of support regions for the flux approximation on the edges sharing a vertex. One of the limitations of this original formulation is the difficulty in dealing with high anisotropy ratio tensors due to its triangular support, then, to overcome this restriction, some FPS formulations were developed, starting with the original MPFA-FPS, by Edwards and Zheng (2008).

One of these FPS variants is the MPFA-D, which uses the so called “diamond stencil” and which was presented by Gao and Wu (2010) and further adapted for the simulation of two-phase flow in petroleum reservoirs by Contreras (2012). This method can handle highly heterogeneous and anisotropic domains by using general polygonal meshes. These are very important characteristics because the permeability, for example, is a property that can vary many orders of magnitude in a short stretch of the domain (GEIGER et al., 2004; CARVALHO, 2005). Moreover, since the sedimentary layers can be deposited in different ways giving different preferential directions for the flow of fluids, the porous media should be treated preferentially as anisotropic systems (CARVALHO, 2005).

In context of solving the hyperbolic transport equation, the First Order Upwind Method (FOUM) has good properties of monotonicity and mildness in regions close to shock, although the numerical diffusion associated with it reduces its accuracy (CARVALHO, 2005). In this formulation, a property value on a face is calculated from the value on the center of the cell which is upstream with respect to the fluid flow.

1.1 Objectives

The objective of this researching work is to develop and implement a numerical scheme to perform 2-D simulations of one-phase and two-phase flows in naturally fractured reservoirs that can deal with any permeability tensors and general polygonal meshes, by using the MPFA-D (applied for the first time in this context), the HyG and the FOUM. The specific objectives of this work are:

1) Develop and implement, in the MATLAB® environment, a programing tool to generate computational hybrid-grids from original grids created by a mesh generation software, as a strategy to handle the fractures.
2) Apply properly the MPFA-D on the created computational hybrid-grids to solve the pressure equation in fractured domains.
3) Apply properly the FOUM, in its implicit and explicit versions, on the created computational hybrid-grids to solve the saturation equation in fractured domains.

1.2 Text Organization

This text is organized in five chapters. In this first chapter, the problem to be studied is presented as well as a brief history of the approaches already used on it and the chosen strategy for this work. In the second chapter, it is presented the mathematical model for the phenomenon studied here, beginning with some simplifying assumptions, followed by some fundamental concepts about oil reservoirs, what is followed by the development of the pressure and saturation equations and the boundary conditions necessary to define the problem. In the third chapter, it is presented the numerical formulation, beginning with a generic algorithm, followed, in this order, by the MPFA-D development, a very brief explanation about the MPFA-O, the FOUM development, in its explicit and implicit versions, and the HyG development. In the fourth chapter, the results of some performed tests and their discussions are presented. The fifth chapter has the conclusions about this work. Finally, the bibliography used here is presented.

2 MATHEMATICAL MODEL

This section presents the mathematical model used in this work to describe the two-phase flow in porous media, including major assumptions, some fundamental concepts, the governing equations and the auxiliary conditions.

2.1 Assumptions

Fluid flow in porous media is a very complex phenomenon, which would lead us to a complex mathematical model, so, aiming to simplify the model to be studied, the following assumptions were considered:

1. Two-phase flow: oil (o) and water (w).
2. Immiscible and incompressible flow.
3. Fully saturated non-deformable rock.
4. Thermal, chemical and capillary effects are neglected.
5. Dispersion and adsorption effects are neglected.
6. Darcy's law is applicable.

2.2 Concepts

This subsection briefly presents some fundamental concepts associated to fluid flow in porous media and that are important to the comprehension of the mathematical model.

2.2.1 Rock and Fluid Properties

Oil reservoirs are porous rock in whose pores are accumulated the fluids. Some of these pores are isolated, while others are interconnected. The ratio of pore volume in a rock sample to the total volume of this rock sample is called porosity (ϕ). Two types of porosity can be calculated, the total porosity, which considers all the pores of the rock sample, and the effective porosity, which account only the interconnected ones (ERTEKIN; ABOU-KASSEM; KING, 2001). In the remainder of this text, the term porosity is used to refer to the effective porosity, because it indicates, the capacity of the reservoir to accumulate fluids that can be displaced (exploitable fluids).

Considering that the pore volume is completely fulfilled by the fluids (or phases), the saturation of a phase i (S_i) is the ratio of the total pore volume which is fulfilled by the phase i. Therefore, the sum of the saturations of all phases needs to be equal to 1.

$$\sum_i S_i = 1 \quad \left(\text{with, under our assumptions, } i = w, o\right) \tag{2.1}$$

As the scope of this work is oil (o) and water (w) two-phase flow, it is important to define the irreducible water saturation (S_{wi}), which is the saturation bellow which the water can not be displaced anymore in drainage processes due to the rock-fluid interactions. A similar effect is observed to the oil in imbibition processes and this minimum limit value is called residual oil saturation (S_{or}).

Permeability is the capacity of a porous medium to transmit fluids through its interconnected pores. If the porous medium is completely saturated by only one phase, this capacity is called absolute permeability, but if there is more than one phase saturating the pores, it is called the effective permeability of each phase (ERTEKIN; ABOU-KASSEM; KING, 2001). The ratio between the effective permeability of a phase i and the absolute permeability of the case in which the porous medium would be completely saturated by this phase i is called relative permeability of this phase (k_{ri}). In this work, Brooks and Corey type functions are used (CHEN; HUAN; MA, 2006; KOZDON; MALLISON; GERRITSEN, 2011; SOUZA, 2015) and the relative permeability is a function of the fluid saturation defined, in this work, for our two phases (oil and water), by:

$$k_{rw} = \left(S_n\right)^{n_w}; \quad k_{ro} = \left(1 - S_n\right)^{n_o} \tag{2.2}$$

where n_w and n_o are exponents that can assume different values (KOZDON; MALLISON; GERRITSEN, 2011; SOUZA, 2015) and S_n is the normalization of the wetting phase saturation with respect to the irreducible water saturation (S_{wi}) and the residual oil saturation (S_{or}). It is defined as (CHEN; HUAN; MA, 2006):

$$S_n = \frac{S_w - S_{wi}}{1 - S_{wi} - S_{or}} \tag{2.3}$$

A rock sample, however, may be more permeable to the flow in one direction than in another, indicating the existence of anisotropy. That is why the permeability is generally described as a tensor, which can be represented as a set of orthogonal vectors or as a symmetric matrix. In 2-D and using Cartesian coordinates, the permeability tensor would be (SOUZA, 2015):

$$\underset{\sim}{K}(\vec{x}) = \begin{bmatrix} K_{xx} & K_{xy} \\ K_{xy} & K_{yy} \end{bmatrix} \tag{2.4}$$

where $\vec{x}$ is the position vector. The full tensor pressure equation is assumed to be elliptic and the permeability tensor must satisfy the following ellipticity condition (EDWARDS; ROGERS, 1998):

$$K_{xy}^2 \leq K_{xx}K_{yy} \tag{2.5}$$

Be the fluid a continuous medium, in which any property of it is defined in any point. Be m the mass and V the volume of a fluid sample. The density (ρ) or the specific mass is defined as (FOX; PRITCHARD; McDONALD, 2010):

$$\rho = \lim_{\delta V \to V^r} \frac{\delta m}{\delta V} \tag{2.6}$$

where V^r is the representative elementary volume above which the density becomes stable, i.e. an average defined value can be deterministically determined.

The viscosity (μ) is the measure of the resistance of the fluid to the flow. This property relates the shear stress applied to a fluid and the gradient of the velocity acquired by it as result of the load (FOX; PRITCHARD; McDONALD, 2010).

The mobility of a phase i (λ_i) is the measure of how mobile this phase is in the presence of other phases. The higher the relative permeability of a phase, the more mobile is that phase. On the other hand, the more viscous is a fluid, the less mobile it is. Thus, the mobility of a phase i is defined as (FANCHI, 2005):

$$\lambda_i = \frac{k_{ri}}{\mu_i} \tag{2.7}$$

The total mobility (λ), in the case in which the capillarity effects are neglected, is defined as the sum of the mobilities of all the phases present in the medium:

$$\lambda = \sum_i \lambda_i \tag{2.8}$$

2.2.2 Darcy's Law

In 1856, Henry Darcy investigated the flow of water in vertical homogeneous sand filters (Figure 1) in connection with the fountains of the city of Dijon, France. From his experiments, Darcy concluded that the rate of flow (volume per time) q is proportional to the cross-sectional area A available to the flow, proportional to the pressure difference $h_1 - h_2$ and inversely proportional to the length of the porous media sample, L.

Figure 1 – Sand filter scheme of the experiment of Henry Darcy.

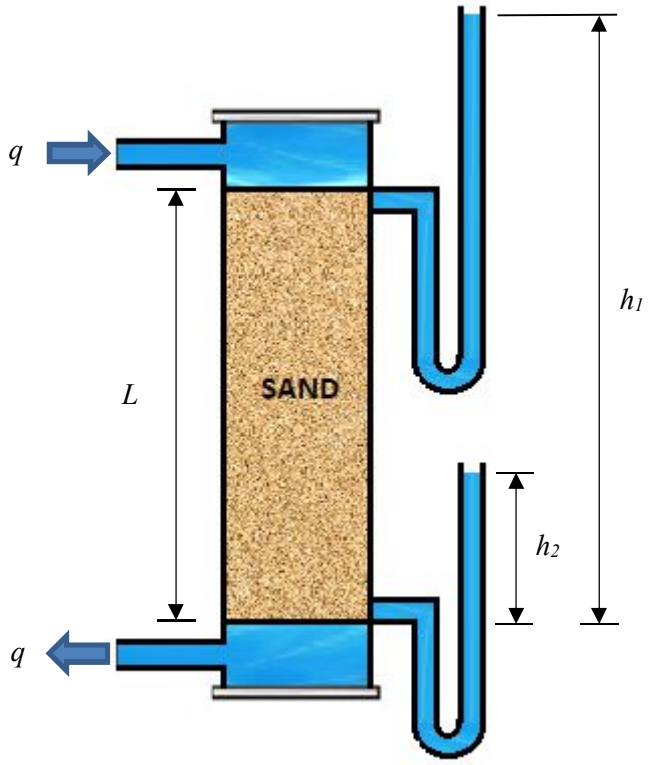

Source: Author.

By combining the evidences described above and by using K as a proportionality factor, the following relation can be obtained (BEAR, 1972; ROSA; CARVALHO; XAVIER, 2006):

$$q = KA\frac{h_1 - h_2}{L} \tag{2.9}$$

Despite being an empiric law, later studies led to a general form to the Darcy's law to a phase i in presence of other phases, which is largely used in reservoir simulation (BEAR, 1972; PEACEMAN, 1977; EWING, 1983):

$$\vec{v}_i = \frac{q_i}{A} = -\lambda_i \underset{\sim}{K}\left(\vec{\nabla} p_i - \rho_i \vec{g}\right) \tag{2.10}$$

where $\vec{v}_i$ is the velocity of the phase, $\vec{\nabla}$ is the gradient operator, p_i is the pressure of the phase i, $\vec{g}$ is the vector of gravity acceleration directed downward and $\underset{\sim}{K}$ is the absolute permeability. Neglecting the gravity and capillarity effects, it becomes:

$$\vec{v}_i = -\lambda_i \underset{\sim}{K} \vec{\nabla} p \tag{2.11}$$

where p is the global pressure. It is also important to define the total velocity as the sum of the velocities of all phases:

$$\vec{v} = \sum_i \vec{v}_i \tag{2.12}$$

2.2.3 Fractional flow

The fractional flow of the phase i can be defined, for the case without gravity and capillarity effects, as (CHEN; HUAN; MA, 2006):

$$f_i = \frac{\lambda_i}{\lambda} \tag{2.13}$$

2.3 Governing Equations

This section briefly presents Equations used to model the two-phase flow (oil and water) in heterogeneous and anisotropic porous media. The mathematical development begins at the mass conservation law (BEAR, 1972) for the phase i, defined as:

$$\phi\rho_i \frac{\partial S_i}{\partial t} + \rho_i \vec{\nabla} \cdot \vec{v}_i = q_i \tag{2.14}$$

in which t stands for time and q_i for the source term of the phase i.

2.3.1 Pressure Equation

Writing Equation (2.14) for both phases and adding them, the following expression is obtained:

$$\phi \frac{\partial \left(S_w + S_o\right)}{\partial t} + \vec{\nabla} \cdot \left(\vec{v}_w + \vec{v}_o\right) = \frac{q_w}{\rho_w} + \frac{q_o}{\rho_o} \tag{2.15}$$

Applying the restriction from Equation (2.1) to eliminate the saturation and using the definition from Equation (2.12) for the total velocity, it is obtained:

$$\vec{\nabla} \cdot \vec{v} = \frac{q_w}{\rho_w} + \frac{q_o}{\rho_o} \tag{2.16}$$

Defining specific total flow rate as $Q = Q_w + Q_o$, where $Q_i = q_i/\rho_i$ (with $i = w,o$), it is possible to write the elliptic pressure equation (PEACEMAN, 1977; EDWARDS; ROGERS, 1998; CARVALHO et al., 2005; CONTRERAS et al., 2016):

$$\vec{\nabla} \cdot \vec{v} = Q \quad (\text{with } \vec{v} = -\lambda \underset{\sim}{K} \vec{\nabla} p) \tag{2.17}$$

Moreover, $\lambda=\lambda_w+\lambda_o$ is the total mobility - see Equation (2.8) -, the expression for $\vec{v}$ comes from the Darcy's Law - see Equation (2.11) - and p is the global pressure, neglecting capillarity effects.

2.3.2 Saturation Equation

Because of the restriction given by Equation (2.1), Equation (2.14) can be written just for the water phase (PEACEMAN, 1977; CARVALHO et al., 2005; CHEN; HUAN; MA, 2006; CONTRERAS et al., 2016). For this, Equation (2.11) is written for both phases, each one multiplied by the mobility of the other phase, to obtain the same expression:

$$\lambda_w \vec{v}_o = \lambda_o \vec{v}_w = -\lambda_w \lambda_o \underset{\sim}{K} \vec{\nabla} p \tag{2.18}$$

Then:

$$\lambda_w \vec{v}_o - \lambda_o \vec{v}_w = 0 \tag{2.19}$$

But $\vec{v}_o = \vec{v} - \vec{v}_w$, then:

$$\lambda_w \left(\vec{v} - \vec{v}_w \right) - \lambda_o \vec{v}_w = 0 \tag{2.20}$$

Rearranging:

$$\lambda_w \vec{v} = \left(\lambda_w + \lambda_o \right) \vec{v}_w = \lambda \vec{v}_w \tag{2.21}$$

Then, the water phase velocity is defined as:

$$\vec{v}_w = \frac{\lambda_w}{\lambda} \vec{v} = f_w \vec{v} \tag{2.22}$$

Then, Equation (2.14) can be written for the water phase as:

$$\phi \frac{\partial S_w}{\partial t} + \vec{\nabla} \cdot \left(f_w \vec{v} \right) = Q_w \tag{2.23}$$

This Equation (2.23) is the hyperbolic saturation equation. Equations (2.17) and (2.23) are coupled by the total velocity field $\vec{v}$ (PEACEMAN, 1977).

2.3.3 Initial and Boundary Conditions

In order to get a complete description of the problem, it is necessary to define appropriate auxiliary, initial and boundary, conditions. In this case, considering a domain Ω, its contour Γ is defined as:

$$\Gamma = \Gamma_D \cup \Gamma_N \cup \Gamma_P \cup \Gamma_I \tag{2.24}$$

where Γ_D and Γ_N represent the boundaries with prescribed pressures (Dirichlet boundary conditions), and prescribed fluxes (Neumann boundary conditions), respectively, and Γ_P and Γ_I represent the production and injection wells, respectively. Therefore, these auxiliary conditions are typically given by (AZIZ; SETTARI, 1979; CONTRERAS et al., 2016):

$$\begin{aligned} &p(\vec{x},t) = g_D && \text{on } \Gamma_D \times [0,t] \\ &\vec{v}\cdot\vec{n} = g_N && \text{on } \Gamma_N \times [0,t] \\ &S_w(\vec{x},t) = \overline{S}_w && \text{on } \Gamma_I \times [0,t] \\ &S_w(\vec{x},0) = \overline{S}_w^0 && \text{on } \Omega \end{aligned} \tag{2.25}$$

where $\vec{x}$ represents the position vector, t is the time variable, g_D is a scalar function for pressure and g_N is a scalar function for flux. Moreover, $\vec{n}$ is the outward unitary normal vector to the control surface, $\vec{v}$ is the total velocity and $\overline{S}_w$ is the prescribed water saturation on an injection well. Beyond this, pressure or flux can be prescribed in the wells, respectively, as $\int_{\Gamma_Z} \vec{v}\cdot\vec{n}\ \partial\Gamma_Z = g_{Z,1}$ or $p(\vec{x},t) = g_{Z,2}$, with $Z=I,P$; where $g_{Z,1}$ and $g_{Z,2}$ are scalar functions for flux and pressure, respectively.

3 NUMERICAL FORMULATION

The complexity of the fluid flow in reservoirs problem makes very difficult or even impossible to obtain analytical solutions. The experimental approach is also unfeasible, that is why it is necessary to use numerical formulations to find the solutions for this type of problems (CHEN; HUAN; MA, 2006; SOUZA, 2015). This section presents the numerical strategy used in this work.

The problem described by Equations (2.17) and (2.23), with their initial and boundary conditions given by Equation (2.25), is solved through two different types of segregated formulations, the Implicit Pressure and Explicit Saturation Scheme (IMPES) (CHEN; HUAN; MA, 2006; AHMED et al., 2015) or the Sequential Implicit Scheme (SEQ) (HOTEIT; FIROOZABADI, 2008; BRUM, 2016).

The numerical formulation was implemented in MATLAB® (an environment that allows easy prototyping and have wide library of functions), modifying and extending some codes developed by Souza (2015) and Contreras et al. (2016), in the PADMEC researching group of UFPE. The mesh generation was made by using the free software GMSH (GEUZAINE and REMACLE, 2009). The visualization of the result pressure and saturation fields was made by using VisIt® (VISIT USER'S MANUAL, 2005) and the graphs were made by using MATLAB®.

3.1 Coupling Strategy

Both schemes, IMPES or SEQ, start with a known saturation distribution, from which the total mobilities throughout the domain are calculated - see Equations (2.2), (2.3), (2.7) and (2.8). Using these mobilities as input, Equation (2.17), the pressure equation, is solved by an implicit formulation. With the pressure distribution calculated from Equation (2.17), the Darcy velocities throughout the domain are calculated and used as input to Equation (2.23), the saturation equation, which is solved by an explicit formulation, in the case of IMPES, or by an implicit one, in the case of SEQ, case in which, to solve the nonlinear system of equations, an iterative method was used (see Figure 2). Both the implicit and the explicit formulations are detailed in section 3.3. In turn, the saturation calculated from Equation (2.23) is used to recalculate the mobilities to be used again as inputs to update the pressure field by Equation (2.17).

In these segregated formulations, this looping procedure is repeated until it reaches the previously set final time of simulation (t_F) (see Figure 2).

Figure 2 – Pressure and Saturation coupling strategy in a segregated formulation.

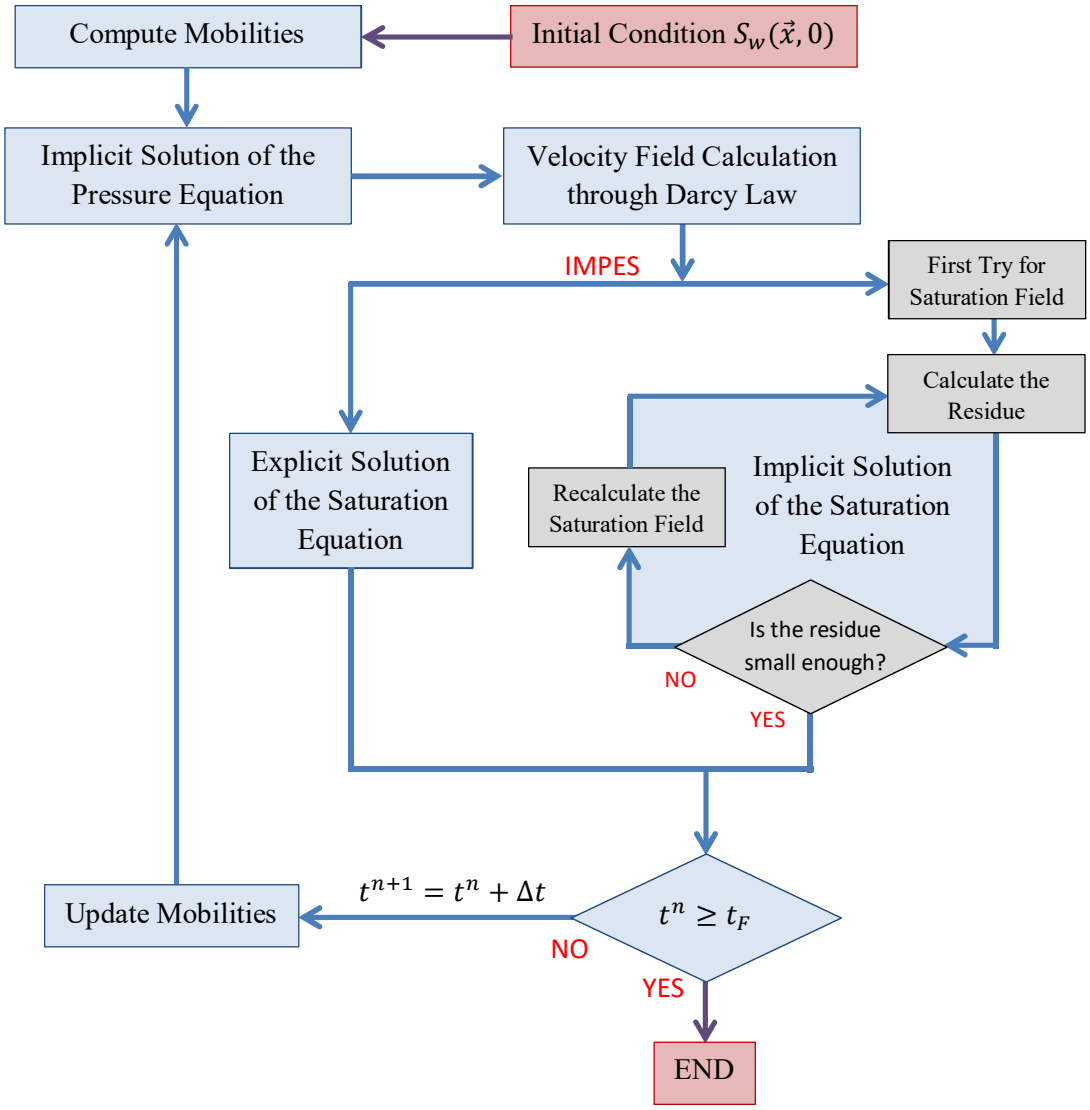

Source: Author.

3.2 Pressure Equation

By integrating Equation (2.17) on a domain Ω (Figure 3.a), the following equation is obtained:

$$\int_{\Omega} \vec{\nabla} \cdot \vec{v} \; \partial\Omega = \int_{\Omega} Q \; \partial\Omega \tag{3.1}$$

and by the Gauss Divergence Theorem, it becomes:

$$\int_{\partial\Omega} \vec{v} \cdot \vec{n} \; \partial\Gamma = \int_{\Omega} Q \; \partial\Omega \tag{3.2}$$

where $\vec{n}$ is the outward unitary normal vector to the control surface Γ. Discretizing the domain Ω with a mesh, as shown in Figure 3.b, it is possible to write, for each grid cell, by using the mean value theorem, the following expression:

$$\sum_{j\in\Gamma_k} \vec{v}_j \cdot \vec{N}_j = \bar{Q}_k \Omega_k \tag{3.3}$$

where $\bar{Q}_k$ is the mean source term, Ω_k is the volume (or area in 2-D) and Γ_k is the set of edges of the *k*-th grid-cell.

Figure 3 – Generic domain: (a) continuous domain with its boundary conditions; (b) generic mesh on the computational domain.

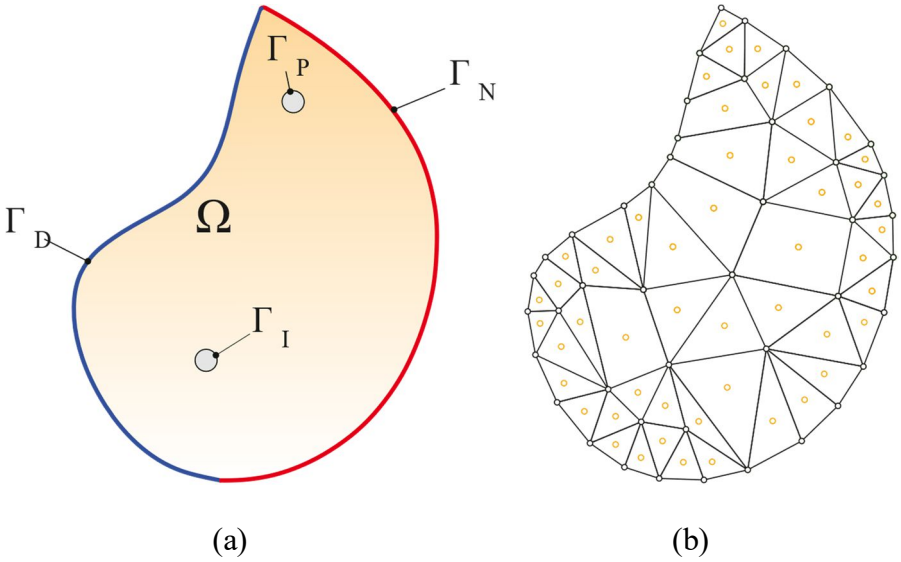

(a) (b)

Source: Author.

3.2.1 Multipoint Flux Approximation Variant with "Diamond" Stencil (MPFA-D)

The flux expression in Equation (3.3) is obtained through the MPFA-D, initially proposed by Gao and Wu (2010) and further developed by Contreras et al. (2016) and extended to fractured porous media in the present work.

Aiming to obtain the expression for the flux crossing one edge, it is necessary to highlight the local set of grid cells around this edge and construct the MPFA-D stencil, as depicted in Figure 4. Consider an edge defined by the nodes *I* and *J*, $\hat{L}$ and $\hat{R}$ denote the barycenters (or collocation points) of the neighbor control volumes (*CV*s) to the left and to the

right of the edge, respectively. The segments $\overrightarrow{IJ}$ and $\overrightarrow{JI}$ are the faces of the cells $\hat{L}$ and $\hat{R}$, respectively. $\vec{N}_{IJ} = \Re\overrightarrow{IJ}$ and $\vec{N}_{JI} = \Re\overrightarrow{JI}$, such that $\vec{N}_{IJ} = -\vec{N}_{JI}$, are the length normal vectors to edges $\overrightarrow{IJ}$ and $\overrightarrow{JI}$, respectively, and $\Re$ is a $\pi/2$ rotation matrix (see Figure 4). The heights of the barycenters to the edge are denoted as $h_{IJ}^{\hat{L}}$ and $h_{JI}^{\hat{R}}$ for the cells $\hat{L}$ and $\hat{R}$, respectively (see Figure 4). $\underset{\sim}{K}(\hat{L}) = \underset{\sim}{K}_{\hat{L}}$ is the permeability of the cell to the left of the considered edge (analogous to the right one).

Figure 4 – Local diagram of a part of an arbitrary polygonal mesh, highlighting the "diamond stencil": $I\hat{R}J\hat{L}$.

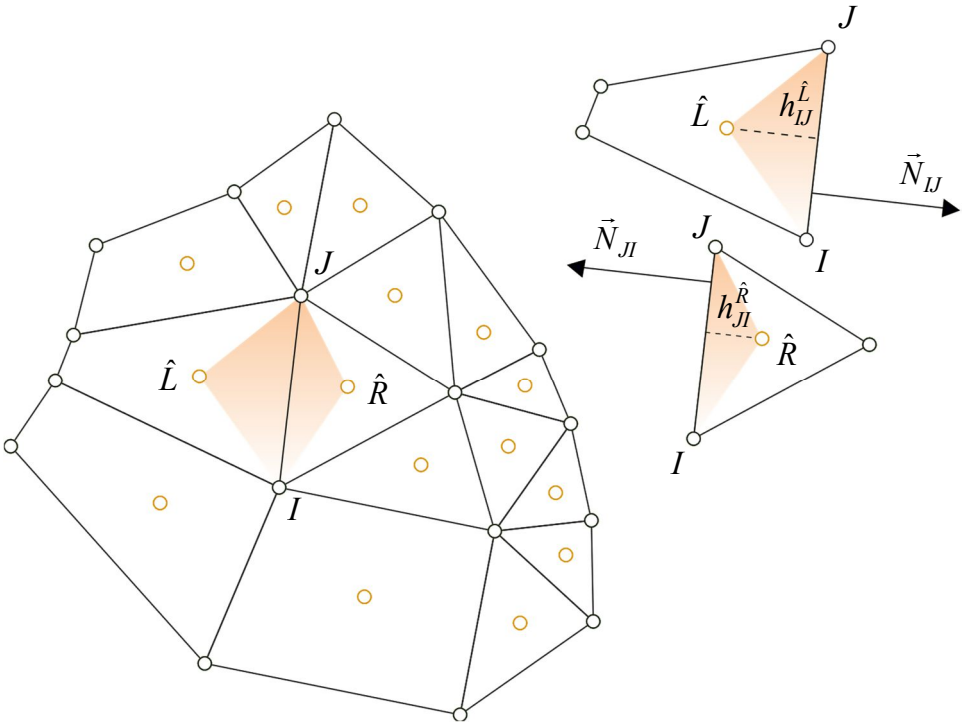

Source: Author.

Considering that $p_{\hat{L}}$ and $p_{\hat{R}}$ are the pressure approximations, respectively, on the left and right *CV*s, and that p_I and p_J are the pressure approximations on the edge vertices, the development of the MPFA-D flux expression can be initiated by the following lemma.

Lemma 1

Let $\triangle OPQ$ be a triangle with the vertices O, P, Q ordered counterclockwise. So, for a function u defined on $\triangle OPQ$:

$$\nabla u \simeq \frac{1}{2S_{\triangle OPQ}}\left[\left(u_P - u_O\right)\Re\overrightarrow{OQ} - \left(u_Q - u_O\right)\Re\overrightarrow{PO}\right] \tag{3.4}$$

and:

$$\nabla u \simeq \frac{\overrightarrow{PQ}}{\left|PQ\right|^2}\left(u_Q - u_P\right) + \frac{\Re\overrightarrow{PQ}}{\left|PQ\right|^2}\left[\left(u_P - u_O\right)\cot\angle PQO + \left(u_Q - u_O\right)\cot\angle OPQ\right] \tag{3.5}$$

where $S_{\triangle OPQ}$ is the area of $\triangle OPQ$, u_i (with $i = O,P,Q$) is the value of the function u on the vertices of the triangle, and the rotation matrix $\Re$ is:

$$\Re = \begin{bmatrix} 0 & 1 \\ -1 & 0 \end{bmatrix} \tag{3.6}$$

So, the estimated pressure gradient on the control volumes to the left ($\hat{L}$) and to the right ($\hat{R}$) (Figure 4) are defined, respectively, as:

$$\nabla p_{IJ}^{\hat{L}} \simeq \frac{\overrightarrow{IJ}}{\left|IJ\right|^2}\left(p_J - p_I\right) + \frac{\vec{N}_{IJ}}{\left|IJ\right|^2}\left[\frac{\overrightarrow{J\hat{L}}\cdot\overrightarrow{JI}}{h_{IJ}^{\hat{L}}\left|IJ\right|}\left(p_I - p_{\hat{L}}\right) + \frac{\overrightarrow{I\hat{L}}\cdot\overrightarrow{IJ}}{h_{IJ}^{\hat{L}}\left|IJ\right|}\left(p_J - p_{\hat{L}}\right)\right] \tag{3.7}$$

$$\nabla p_{IJ}^{\hat{R}} \simeq \frac{\overrightarrow{JI}}{\left|IJ\right|^2}\left(p_I - p_J\right) + \frac{\vec{N}_{JI}}{\left|IJ\right|^2}\left[\frac{\overrightarrow{J\hat{R}}\cdot\overrightarrow{JI}}{h_{JI}^{\hat{R}}\left|IJ\right|}\left(p_I - p_{\hat{R}}\right) + \frac{\overrightarrow{I\hat{R}}\cdot\overrightarrow{IJ}}{h_{JI}^{\hat{R}}\left|IJ\right|}\left(p_J - p_{\hat{R}}\right)\right] \tag{3.8}$$

Considering the triangle $\triangle\hat{L}IJ$ (Figure 4), the flow crossing the control surface IJ, with respect to the cell to the left, can approximated as:

$$\vec{v}_{IJ}^{\hat{L}}\cdot\vec{N}_{IJ} \simeq -\lambda_{IJ}\left\{K_{IJ_{\hat{L}}}^{(n)}\left[\frac{\overrightarrow{J\hat{L}}\cdot\overrightarrow{JI}}{h_{IJ}^{\hat{L}}\left|IJ\right|}\left(p_I - p_{\hat{L}}\right) + \frac{\overrightarrow{I\hat{L}}\cdot\overrightarrow{IJ}}{h_{IJ}^{\hat{L}}\left|IJ\right|}\left(p_J - p_{\hat{L}}\right)\right] + K_{IJ_{\hat{L}}}^{(t)}\left(p_J - p_I\right)\right\} \tag{3.9}$$

with:

$$K_{IJ_{\hat{L}}}^{(n)} = \frac{\left(\vec{N}_{IJ}\right)^T \underset{\sim}{K}_{\hat{L}}\left(\vec{N}_{IJ}\right)}{\left|\overrightarrow{IJ}\right|^2};\quad K_{IJ_{\hat{L}}}^{(t)} = \frac{\left(\vec{N}_{IJ}\right)^T \underset{\sim}{K}_{\hat{L}}\left(\overrightarrow{IJ}\right)}{\left|\overrightarrow{IJ}\right|^2} \tag{3.10}$$

The term λ_{IJ} is the mobility value calculated on the edge IJ. Therefore, Equation (3.9) can be written as:

$$\frac{h_{IJ}^{\hat{L}}}{\lambda_{IJ}K_{IJ_{\hat{L}}}^{(n)}}\vec{v}_{IJ}^{\hat{L}}\cdot\vec{N}_{IJ} \simeq -\frac{1}{\left|IJ\right|}\left[\frac{\overrightarrow{J\hat{L}}\cdot\overrightarrow{JI}}{\left|IJ\right|}\left(p_I - p_{\hat{L}}\right) + \frac{\overrightarrow{I\hat{L}}\cdot\overrightarrow{IJ}}{\left|IJ\right|}\left(p_J - p_{\hat{L}}\right)\right] - h_{IJ}^{\hat{L}}\frac{K_{IJ_{\hat{L}}}^{(t)}}{K_{IJ_{\hat{L}}}^{(n)}}\left(p_J - p_I\right) \tag{3.11}$$

The same expression can be written for the grid cell to the right:

$$\frac{h_{IJ}^{\hat{R}}}{\lambda_{IJ}K_{IJ_{\hat{R}}}^{(n)}}\vec{v}_{IJ}^{\hat{R}}\cdot\vec{N}_{IJ}\simeq-\frac{1}{|IJ|}\left[\frac{\overrightarrow{I\hat{R}}\cdot\overrightarrow{IJ}}{|IJ|}\left(p_J-p_{\hat{R}}\right)+\frac{\overrightarrow{J\hat{R}}\cdot\overrightarrow{JI}}{|IJ|}\left(p_I-p_{\hat{R}}\right)\right]-h_{IJ}^{\hat{R}}\frac{K_{IJ_{\hat{R}}}^{(t)}}{K_{IJ_{\hat{R}}}^{(n)}}\left(p_I-p_J\right) \tag{3.12}$$

By the imposition of flux continuity, it comes:

$$\vec{v}_{IJ}^{\hat{L}}\cdot\vec{N}_{IJ}=-\vec{v}_{IJ}^{\hat{R}}\cdot\vec{N}_{IJ}=\vec{v}_{IJ}\cdot\vec{N}_{IJ} \tag{3.13}$$

Subtracting Equations (3.12) – (3.13) and making the substitution indicated in Equation (3.14), and after some algebraic manipulation, the unique flux equation can be rewritten as:

$$\vec{v}_{IJ}\cdot\vec{N}_{IJ}=\tau_{IJ}\left[p_{\hat{R}}-p_{\hat{L}}-\upsilon_{IJ}\left(p_J-p_I\right)\right] \tag{3.14}$$

where:

$$\tau_{IJ}=-\lambda_{IJ}\frac{K_{IJ_{\hat{L}}}^{(n)}K_{IJ_{\hat{R}}}^{(n)}}{K_{IJ_{\hat{L}}}^{(n)}h_{JI}^{\hat{R}}+K_{IJ_{\hat{R}}}^{(n)}h_{IJ}^{\hat{L}}}\left|\overrightarrow{IJ}\right| \tag{3.15}$$

$$\upsilon_{IJ}=\frac{\overrightarrow{\hat{L}\hat{R}}\cdot\overrightarrow{IJ}}{\left|\overrightarrow{IJ}\right|^2}-\frac{1}{\left|\overrightarrow{IJ}\right|}\left(\frac{K_{IJ_{\hat{L}}}^{(t)}}{K_{IJ_{\hat{L}}}^{(n)}}h_{IJ}^{\hat{L}}+\frac{K_{IJ_{\hat{R}}}^{(t)}}{K_{IJ_{\hat{R}}}^{(n)}}h_{JI}^{\hat{R}}\right) \tag{3.16}$$

The expression for the flux crossing the edge *IJ* - see Equation (3.14) - is dependent of the pressures on the elements to the left and to the right of *IJ* and on the vertices *I* and *J*, then, to obtain a completely cell-centered formulation, it is necessary interpolate the pressures on the vertices. A strategy for realizing these interpolations is presented later in this text. Note that the tangential term, shown in Equation (3.16), disappears from Equation (3.14) when the permeability tensor is K-orthogonal, what makes, in these cases, this MPFA-D scheme becomes a two-point flux approximation formulation (TPFA) (GAO; WU, 2010).

3.2.2 Boundary Treatment

The flux expression over boundaries with prescribed pressures is given by:

$$\vec{v}_{IJ}\cdot\vec{N}_{IJ}=-\lambda_{\hat{L}}\frac{K_{IJ_{\hat{L}}}^{(n)}}{h_{IJ}^{\hat{L}}\left|\overrightarrow{IJ}\right|}\left[\left(\overrightarrow{J\hat{L}}\cdot\overrightarrow{JI}\right)g_D^I+\left(\overrightarrow{I\hat{L}}\cdot\overrightarrow{IJ}\right)g_D^J-\left|\overrightarrow{IJ}\right|^2p_{\hat{L}}\right]-\left(g_D^J-g_D^I\right)K_{IJ_{\hat{L}}}^{(t)} \tag{3.17}$$

where $g_D^J = p_J$, $g_D^I = p_I$ are known. Whenever there is a prescribed flux over the boundaries, we can write:

$$\vec{v}_{IJ} \cdot \vec{N}_{IJ} = g_N \left| \overrightarrow{IJ} \right| \tag{3.18}$$

where g_N is this prescribed flux.

3.2.3 Face Mobility Approximation

It is necessary to define how to calculate the term λ_{IJ} in Equation (3.15). In many applications, this value is assumed to be the mobility on the *CV* which is upstream with respect to the flow (AZIZ; SETTARI, 1979; HURTADO, 2005; KOZDON; MALLISON; GERRITSEN, 2011; SOUZA, 2015), but in the works of Hurtado (2005) and Souza et al. (2018), who have studied more properly this issue, this approach is overcome by the linear approximations (which calculate some average of the mobilities on the *CV*s neighboring the face *IJ*, without considering the flow direction), which present, in general, better results.

The linear approximation of the mobility on *IJ* could be made as some type of volume weighting average of the mobilities on the grid cells neighboring this edge, which had been tried during the development of this work, but returned wrong results, because of the applications to naturally fractured reservoirs. Due to the very small volume (or area, in 2-D) of the fractures cells, any volume weighting would lead a physical incoherence: the mobilities on fractures cells, which are very relevant to the physical phenomenon, would have very small weights on the calculation. That is why the simple arithmetic average between the mobilities on the cells to the left and to the right is used here, as shown in Equation (3.19), this way, if a rock matrix cell and a fracture cell share an edge, they will have the same weight on the calculation.

$$\lambda_{IJ} = \frac{\lambda_{\hat{L}} + \lambda_{\hat{R}}}{2} \tag{3.19}$$

3.2.4 Treatment of Vertex Unknowns

To get a fully cell-centered formulation, it is necessary to obtain the pressures on each node, which are not on Dirichlet boundaries, by interpolation considering a weighted average of the pressures of the primal cells that share that node (Figure 5.a). It is possible to obtain the weights of this interpolation explicitly, avoiding the inversion of local matrices. Following Queiroz et al. (2014) and Contreras et al. (2016), in this work, the LPEW2 (Linear

Preserving Explicit Weighting type 2) of Gao and Wu (2010) was used. The following is a general outline of the path followed to obtain the weights expression according to LPEW2. For more details, see Appendix A.

The first thing to do is to build a dual cell surrounding each node to be interpolated, as shown in Figure 5.a, defined by connecting the auxiliary variables ($\bar{k}$) at the midpoint of each edge which share the node to be interpolated. In Figure 5.a, the node J is shared by n_J cells. But, imposing divergence free, the flow balance on the dual CV is:

$$\sum_{k=1}^{n_J} \vec{v}_{\bar{k}\,\overline{k+1}} \cdot \vec{N}_{\bar{k}\,\overline{k+1}} = 0 \tag{3.20}$$

By the Lemma 1, the expressions for $\vec{v}_{\bar{k}\,\overline{k+1}} \cdot \vec{N}_{\bar{k}\,\overline{k+1}}$ can be written using the values of the pressures on $\bar{k}$, $\overline{k+1}$ and J. Aiming to eliminate these auxiliary variables on the edges it is necessary to impose the flux continuity on the half edges $J\bar{k}$:

$$\vec{v}_{J\bar{k}} \cdot \vec{N}_{J\bar{k}} + \vec{v}_{\bar{k}J} \cdot \vec{N}_{\bar{k}J} = 0 \tag{3.21}$$

These flux expressions can be written, by Lemma 1, using the pressure values on $\bar{k}$, $\hat{k}$, $\hat{k+1}$ and J. Therefore, by Equation (3.21) it is possible to get an expression for the pressure on $\bar{k}$ in function of the pressures on $\hat{k}$, $\hat{k+1}$ and J, to be substituted in Equation (3.20). After some algebraic manipulation, it is possible to write an expression for the pressure on J as a function of the pressures on $\hat{k}$, in the following format:

$$p_J = \sum_{k=1}^{n_J} w_{\hat{k}} p_{\hat{k}} = w_{\hat{1}} p_{\hat{1}} + \cdots + w_{\hat{k-1}} p_{\hat{k-1}} + w_{\hat{k}} p_{\hat{k}} \tag{3.22}$$

where $w_{\hat{k}}$ is the weight assigned to the k-th cell surrounding the shared node - i.e. weight assigned to $p_{\hat{k}}$ in Equation (3.22). Considering the development given by Gao and Wu (2010), and the parameters shown in Figure 5.b, each explicit weight $w_{\hat{k}}$ can be computed as:

$$w_{\hat{k}} = \frac{\overline{\psi}_k}{\sum_{k=1}^{n_J} \overline{\psi}_k};\ k = 1, 2, \ldots, n_J \tag{3.23}$$

Figure 5 – Notation for control volumes surrounding vertex *J*: (a) Nodes and edges surrounding node *J*. (b) Parameters used to calculate the type 2 explicit interpolation weights from Gao and Wu (2010), for the *k*-th cell.

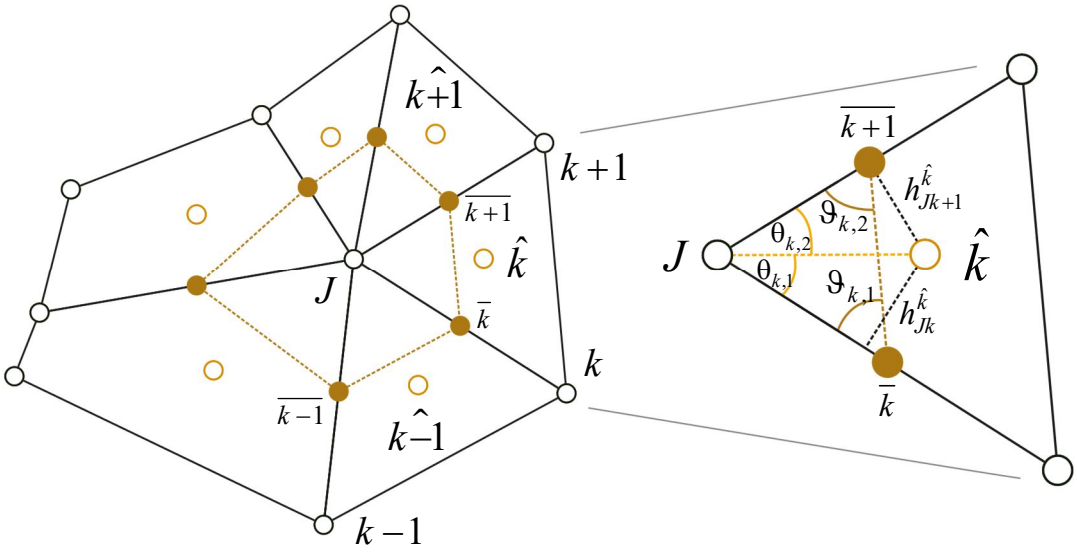

(a) (b)

Source: Author.

where:

$$\bar{\psi}_k = T^{(n)}_{\hat{k},1}\eta_{k,1}\xi_k + T^{(n)}_{\hat{k},2}\eta_{k,2}\xi_{k+1} \tag{3.24}$$

with:

$$\eta_{k,1} = \frac{\left|\overrightarrow{J\bar{k}}\right|}{h^{\hat{k}}_{Jk}}; \quad \eta_{k,2} = \frac{\left|\overrightarrow{J\overline{k+1}}\right|}{h^{\hat{k}}_{Jk+1}} \tag{3.25}$$

and:

$$T^{(n)}_{\hat{k},1} = \lambda_{\bar{k}\overline{k-1}} \frac{\left(\vec{N}_{J\bar{k}}\right)^T \underset{\sim}{K}_{\hat{k}} \left(\vec{N}_{J\bar{k}}\right)}{\left|\overrightarrow{J\bar{k}}\right|^2}; \quad T^{(n)}_{\hat{k},2} = \lambda_{\bar{k}\overline{k+1}} \frac{\left(\vec{N}_{J\overline{k+1}}\right)^T \underset{\sim}{K}_{\hat{k}} \left(\vec{N}_{J\overline{k+1}}\right)}{\left|\overrightarrow{J\overline{k+1}}\right|^2} \tag{3.26}$$

in which $\lambda_{\bar{k}\,\overline{k+1}}$ is the mobility on the half-edge $\overrightarrow{\bar{k}\,\overline{k+1}}$, analogue to $\lambda_{\overline{kk-1}}$. It is also necessary to define ξ_k, for Equation (3.24), as:

$$\xi_k = \frac{\overline{T}^{(t)}_{\hat{k-1}} - \overline{T}^{(t)}_{\hat{k}} + \overline{T}^{(n)}_{\hat{k-1}} \cot \vartheta_{\hat{k-1},1} + \overline{T}^{(n)}_{\hat{k}} \cot \vartheta_{\hat{k},2}}{T^{(n)}_{\hat{k-1},2} \cot \theta_{\hat{k-1},2} + T^{(n)}_{\hat{k},1} \cot \theta_{\hat{k},1} - T^{(t)}_{\hat{k-1},2} + T^{(t)}_{\hat{k},1}} \tag{3.27}$$

with:

$$\begin{aligned} T^{(t)}_{\hat{k},1} &= \lambda_{\overline{k\,k-1}} \frac{\left(\vec{N}_{J\overline{k}}\right)^T \underset{\sim}{K}_{\hat{k}} \left(\overrightarrow{J\overline{k}}\right)}{\left|\overrightarrow{J\overline{k}}\right|^2}; \; T^{(t)}_{\hat{k},2} = \lambda_{\overline{k\,k+1}} \frac{\left(\vec{N}_{J\overline{k+1}}\right)^T \underset{\sim}{K}_{\hat{k}} \left(\overrightarrow{J\overline{k+1}}\right)}{\left|\overrightarrow{J\overline{k+1}}\right|^2}; \\ \overline{T}^{(n)}_{\hat{k}} &= \lambda_{\hat{k}} \frac{\left(\vec{N}_{\overline{k\,k+1}}\right)^T \underset{\sim}{K}_{\hat{k}} \left(\vec{N}_{\overline{k\,k+1}}\right)}{\left|\overrightarrow{\overline{k\,k+1}}\right|^2}; \; \overline{T}^{(t)}_{\hat{k}} = \lambda_{\hat{k}} \frac{\left(\vec{N}_{\overline{k\,k+1}}\right)^T \underset{\sim}{K}_{\hat{k}} \left(\overrightarrow{\overline{k\,k+1}}\right)}{\left|\overrightarrow{\overline{k\,k+1}}\right|^2}; \end{aligned} \tag{3.28}$$

where $\lambda_{\hat{k}}$ is the mobility on k-th cell surrounding J. The angles $\theta_{k,1}$, $\theta_{k,2}$, $\vartheta_{k,1}$ and $\vartheta_{k,2}$ are defined as shown in Figure 5.b. There is a slight modification to be made when the vertex to be interpolated is on the boundary, which is explained in Appendix A.

3.2.5 Multipoint Flux Approximation Variant with "O" Stencil (MPFA-O)

Considering that it is important to compare the applicability of the MPFA-D with more classical methods, the HyG was also coupled with the MPFA-O (AAVATSMARK; BARKVE; MANNSETH, 1998.A; 1998.B; EDWARDS; ROGERS, 1998; SOUZA, 2015) to be applied in some tests. In this method, the flux calculation on the edge IJ (see Figure 6) is made by summing the fluxes calculated through the semi-faces $I\bar{u}$ and $\bar{u}J$.

The flux through $I\bar{u}$ is calculated by using the support regions $\triangle\bar{h}\hat{h}\bar{u}$ and $\triangle\bar{u}\hat{k}\bar{g}$. On the other hand, the flux through $\bar{u}J$ is calculated by using the support regions $\triangle\bar{t}\hat{h}\bar{u}$ and $\triangle\bar{u}\hat{k}\bar{k}$. Note that as the support regions do not include the nodes I and J, the interpolation of their function values, as done in MPFA-D, is avoided. To eliminate the auxiliary variables at the midpoints of the edges sharing I and J, it is necessary to impose the flux continuity in all the semi-faces sharing those nodes. For this, a support region ring (hence the suffix "O") is built surrounding each node (see Figure 6), with which an algebraic equation system is written by the flux continuity imposition on each semi-face. By these equations systems, the auxiliary variables at the midpoints of the edges can be written as function of the variables at the centers of the cells sharing the nodes, then the expressions for the flux crossing through the semi-faces $I\bar{u}$ and $\bar{u}J$ can be written only by cell center variables.

This configuration makes the MPFA-O a Triangle Pressure Support (TPS) formulation, with regions of the domain where the pressure is extrapolated, instead of

interpolated, which leads to a more limited capability to deal with any meshes or permeability tensors, if compared, for example, with MPFA-D, MPFA-Enriched (CHEN et al., 2008) or MPFA-FPS (EDWARDS; ZHENG, 2008), which are FPS formulations.

Figure 6 – Local diagram of a part of an arbitrary polygonal mesh, highlighting the stencil for the MPFA-O.

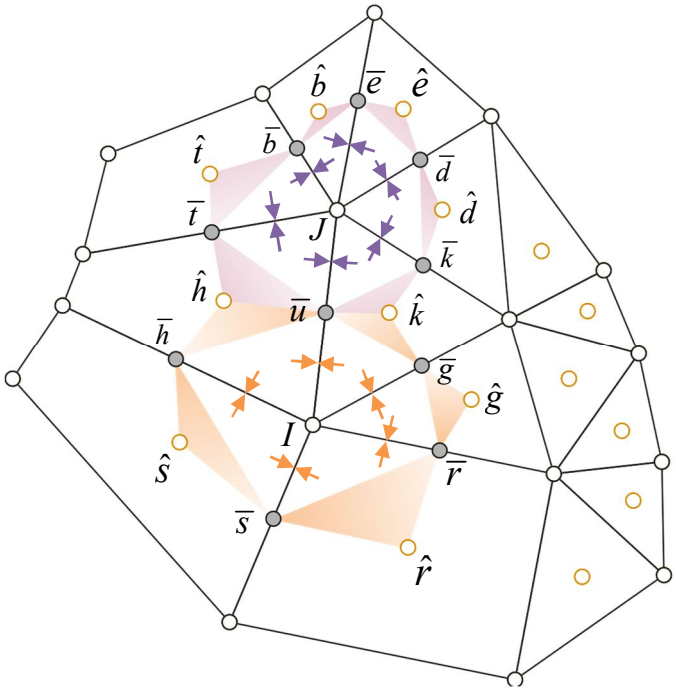

Source: Author.

3.3 Saturation Equation

In this work, two segregated schemes were used to solve the proposed problem: IMPES, in which the saturation equation is calculated explicitly, and SEQ, in which the saturation equation is solved implicitly. In both formulations the discretization is made by the First Order Upwind Method (FOUM).

By integrating Equation (2.23) over *k*-th grid *CV*, the following expression is obtained:

$$\int_{\Omega_k} \phi_k \frac{\partial S_{w(k)}}{\partial t} \partial\Omega_k + \int_{\Omega_k} \vec{\nabla} \cdot \left(f_w \vec{v} \right) \partial\Omega_k = \int_{\Omega_k} Q_{w(k)} \partial\Omega_k \tag{3.29}$$

Using the mean value theorem, the first term becomes:

$$\int_{\Omega_k} \phi_k \frac{\partial S_{w(k)}}{\partial t} \partial\Omega_k \cong \bar{\phi}_k \frac{\Delta \bar{S}_{w(k)}}{\Delta t} \Omega_k \tag{3.30}$$

where $\bar{S}_{w(k)}$ and $\bar{\phi}_k$ are the mean representative values of the water saturation and of the porosity, respectively, in the *k*-th cell, although, from now, these variables will appear in the text without the upper bar. Using again the mean value theorem, the right-hand side term becomes:

$$\int_{\Omega_k} Q_{w(k)} \partial\Omega_k = \bar{Q}_{w(k)} \Omega_k \tag{3.31}$$

From the Gauss Divergence Theorem, the second term becomes:

$$\int_{\Omega_k} \vec{\nabla} \cdot \left(f_w \vec{v} \right) \partial\Omega_k = \int_{\Gamma_k} f_w \vec{v} \cdot \vec{n}_k \partial\Gamma_k \cong \sum_{IJ \in \Gamma_k} \left(f_w \right)_{IJ} \vec{v}_{IJ} \cdot \vec{N}_{IJ} \tag{3.32}$$

in which the term $\left(f_w\right)_{IJ} \vec{v}_{IJ} \cdot \vec{N}_{IJ}$, for an edge *IJ* is computed as the upwind flux, by the following expression:

$$\left(f_w \right)_{IJ} \vec{v}_{IJ} \cdot \vec{N}_{IJ} = \begin{cases} f_{w,\hat{L}} \vec{v}_{IJ} \cdot \vec{N}_{IJ}, & \text{if } \alpha_{IJ} \geq 0 \\ f_{w,\hat{R}} \vec{v}_{IJ} \cdot \vec{N}_{IJ}, & \text{if } \alpha_{IJ} < 0 \end{cases} \tag{3.33}$$

where $f_{w,\hat{L}}$ and $f_{w,\hat{R}}$ are respectively the fractional flows of the cells to the left and to the right of the edge *IJ*, and α_{IJ} is defined as:

$$\alpha_{IJ} = \left(\vec{v}_{IJ} \cdot \vec{N}_{IJ} \right) \left(\frac{\partial f_w}{\partial S_w} \right)_{IJ} \tag{3.34}$$

Using Equations (3.29) to (3.32), it is possible to write the expression for the FOUM:

$$\frac{\Delta S_{w(k)}}{\Delta t} = \frac{1}{\phi_k \Omega_k} \left[\bar{Q}_{w(k)} V_k - \sum_{IJ \in \Gamma_k} \left(f_w \right)_{IJ} \vec{v}_{IJ} \cdot \vec{N}_{IJ} \right] \tag{3.35}$$

The time discretization can be done by using the Euler Explicit Method (TANNEHILL; ANDERSON; PLETCHER, 1997):

$$\frac{S_{w(k)}^{n+1} - S_{w(k)}^{n}}{\Delta t} = \left[\frac{\bar{Q}_{w(k)}}{\phi_k} - \frac{1}{\phi_k \Omega_k} \sum_{IJ \in \Gamma_k} \left(f_w \right)_{IJ} \vec{v}_{IJ} \cdot \vec{N}_{IJ} \right]^n \tag{3.36}$$

Note that in Equation (3.36) the right-hand side is calculated in the time step *n*, so the term $S_{w(k)}^{n+1}$ can be calculated explicitly, using all the information from the previous time step.

This is the strategy used in IMPES scheme and it is conditionally stable, being necessary to satisfy a CFL-type condition (HIRSCH, 1994; SOUZA, 2015) defined for the *k*-th grid cell as:

$$\Delta t_k \leq C \frac{\phi V_k}{\max\limits_{IJ \in \Gamma_k} \left[\left| \left(\frac{\partial f_w}{\partial S_w} \right)_{IJ} \vec{v}_{IJ} \cdot \vec{N}_{IJ} \right| \right] + \bar{Q}_{w(k)} \Omega_k} \tag{3.37}$$

in which C is the Courant number and $(\partial f_w / \partial S_w)_{IJ}$ is the partial derivative of the fractional flow in relation to saturation at the face *IJ*. The global time step is defined as the minimum of all Δt_k:

$$\Delta t = \min_{\Omega_k \in \Omega} \Delta t_k \tag{3.38}$$

Alternatively, in the SEQ formulation the saturation equation is solved implicitly. For this, Equation (3.35), which was written for the *k*-th cell, is rewritten as a matrix equation:

$$\boldsymbol{S}_{\boldsymbol{w}}^{n} + \Delta t \left[\underset{\sim}{G} \right] \boldsymbol{f}_{\boldsymbol{w}}^{n+1} - \boldsymbol{S}_{\boldsymbol{w}}^{n+1} = \boldsymbol{0} \tag{3.39}$$

in which $\boldsymbol{f}_{\boldsymbol{w}}^{n+1}$ and $\boldsymbol{S}_{\boldsymbol{w}}^{n+1}$ are respectively the vectors of the water fractional flow and of the water saturation in each grid cell at the $(n+1)$-th time step. The entries of the matrix $\underset{\sim}{G}$ are defined as:

$$G_{kk} = \frac{1}{\phi_k V_k} \left[\bar{Q}_k \Omega_k - \sum_{IJ \in \Gamma_k} \chi \left(\vec{v}_{IJ} \cdot \vec{N}_{IJ} \right) \right] \tag{3.40}$$

$$G_{ki} = \left(\chi - 1 \right) \frac{\vec{v}_{IJ} \cdot \vec{N}_{IJ}}{\phi_k \Omega_k}; \; IJ = \Gamma_k \cap \Gamma_i \tag{3.41}$$

$$\chi = \begin{cases} 1, \text{ if the } k\text{-th grid cell is the } CV \text{ upwind to } \vec{v}_{IJ} \cdot \vec{N}_{IJ} \\ 0, \text{ if the } i\text{-th grid cell is the } CV \text{ upwind to } \vec{v}_{IJ} \cdot \vec{N}_{IJ} \end{cases} \tag{3.42}$$

in which $\bar{Q}_k$ is the mean representative value of the total source term in the *k*-th cell, which shares the edge *IJ* with the *i*-th cell. To solve the non-linear system of equations, the classical Newton-Raphson (NR) method (BURDEN; FAIRES, 2010) was used, which is an iterative root-finding algorithm. Therefore, to the *j*-th iteration, Equation (3.39) becomes:

$$\boldsymbol{S}_{\boldsymbol{w}}^{n} + \Delta t \left[\underset{\sim}{G} \right] \boldsymbol{f}_{\boldsymbol{w}}^{n+1} \Big|^{j} - \boldsymbol{S}_{\boldsymbol{w}}^{n+1} \Big|^{j} = \boldsymbol{r}^{j} \tag{3.43}$$

in which the convergence criterion, considering a chosen tolerance δ, is:

$$\max(\boldsymbol{r}^j) \leq \delta \tag{3.44}$$

with the value of $\boldsymbol{r}^j$ from Equation (3.43) it is possible to calculate the saturation vector for the $(j+1)$-th iteration as:

$$\boldsymbol{S}_{\boldsymbol{w}}^{n+1}\Big|^{j+1} = \boldsymbol{S}_{\boldsymbol{w}}^{n+1}\Big|^{j} - \underset{\sim}{J}\left(\boldsymbol{S}_{\boldsymbol{w}}^{n+1}\Big|^{j}\right)^{-1} \boldsymbol{r}^j \tag{3.45}$$

where:

$$\underset{\sim}{J}\left(\boldsymbol{S}_{\boldsymbol{w}}^{n+1}\right) = \Delta t\left[\underset{\sim}{G}\right]\left(\underset{\sim}{I}\left[\dot{\boldsymbol{f}}_{\boldsymbol{w}}^{n+1}\right]\right) - \underset{\sim}{I} \tag{3.46}$$

in which $\dot{\boldsymbol{f}}_{\boldsymbol{w}}^{n+1}$ is the vector of the partial derivatives of the fractional flow in relation to saturation in each grid cell, i.e. $\partial f_{w(k)}^{n+1} / \partial S_{w(k)}$ is the k-th entry (relative to the k-th grid cell), in the time step $n+1$ and $\underset{\sim}{I}$ is the identity matrix. The saturation vector calculated by Equation (3.45) is used as input to Equation (3.43) in the $(j+1)$-th iteration.

Although, there is no formal time step restriction for the implicit solution of the saturation equation, if the size of the time step is too big, the accuracy on the solution can be lost (HIRSCH, 1994). Besides, it is important to keep in mind that some instability can also occur due to the segregated character of the SEQ method.

Given the difficulty of determining the maximum feasible time step for the SEQ method, in this work, the calculation of the restricted time step of the explicit case was used as reference also for the implicit case, however using bigger values for the Courant number, in this last case. Furthermore, in the implicit case, if the amount of iterations needed to achieve the condition of Equation (3.44) is bigger than a chosen value, for example, it is possible to decrease the time step and try again, to prevent the iterative process from extending too far.

The time step is clearly more computationally expensive in the implicit scheme than in the explicit scheme, but when the latter one becomes excessively restrictive to the time advance, as in the case of fractured reservoirs, frequently, the implicit scheme becomes more efficient from a computational point of view, because it allows larger steps.

3.4 Hybrid-Grid Method

The geological activities during the formation of the reservoir system may lead to the occurrence of natural fractures in it. In this context, aiming to simulate a domain containing fractures (see Figure 7.a), it is necessary to use a specific strategy to treat this type of entities.

As explained in the introduction of this text, the Hybrid-Grid Method (HyG) was chosen, with due justification, to treat the fractures.

Figure 7 – Fractured domain. (a) Sketch of a domain with fractures (Γ_F). (b) Geometric mesh discretizing the domain, with the edges corresponding to the fractures marked as brown. (c) Computational mesh discretizing the domain, with the expanded fractures as polygonal grid cells.

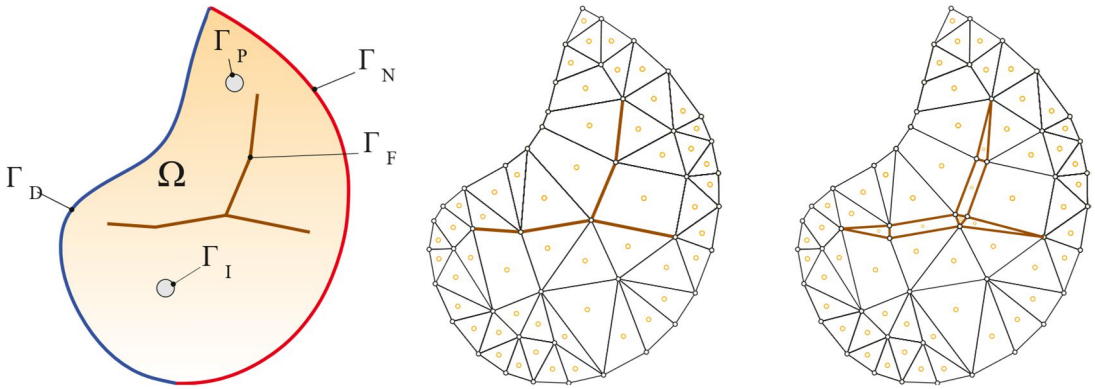

(a) (b) (c)

Source: Author.

This scheme consists on the explicit representation of the fractures, in the geometric mesh, as lower-dimensional entities (lines in 2-D domains or surfaces in 3-D domains, for example – see Figure 7.b) and expand them to the same dimension of the mesh in computational domain (Figure 7.c), so Equations for the fractures and for the rock matrix can be discretized together. Karimi-Fard, Durlofsky and Aziz (2004) presented, in a context of control-volume finite-difference, this strategy to treat fractures, but without call it as Hybrid-Grid. This name was given by Sandve, Berre and Nordbotten (2012), who presented it in the context of a MPFA method, what was followed by Ahmed et al. (2017), who presented a coupling of it with a full-pressure support formulation, the CVD-MPFA.

Although the fractures in the geometric mesh are represented as lower-dimensional entities, the missing transverse dimension is indicated as the fracture aperture which must be previously set for each fracture family, because the construction of the hybrid-grid (the computational grid in which the fractures are dimensionally expanded) is made considering

this parameter. For this work, which uses just 2-D meshes, the hybrid-grid construction was made by following the procedure explained below:

1 – In the vicinity of each fracture-edge (geometric mesh edge representing a fracture), two parallel straight lines must be traced (auxiliary lines), each one at the distance of half of the aperture set for that fracture (Figure 8.a).

2 – If a node is shared by n fracture-edges (with $n > 1$), there will occur n intersections by adjacent auxiliary lines that will correspond to the new points of the computational mesh. In Figure 8.a, node N is shared by three fracture-edges, what lead to the emergence of three new nodes, represented as N', N'' and N'''. So, each point shared by n fracture-edges will become n new points. Assuming that the nodes I and P are shared by two fracture-edges, for example, they become the new nodes I', I'', P' and P'' (Figure 8.b). If the node is shared by only one fracture-edge, it will not occur any intersection and the original node is kept (see node T in Figures 8.a and 8.b).

3 – Connect the points to form the new polygons corresponding to the expanded fractures (Figure 8.b).

Figure 8 – Hybrid-grid construction. (a) Parallel segments tracing and new points determination. (b) Hybrid-grid configuration.

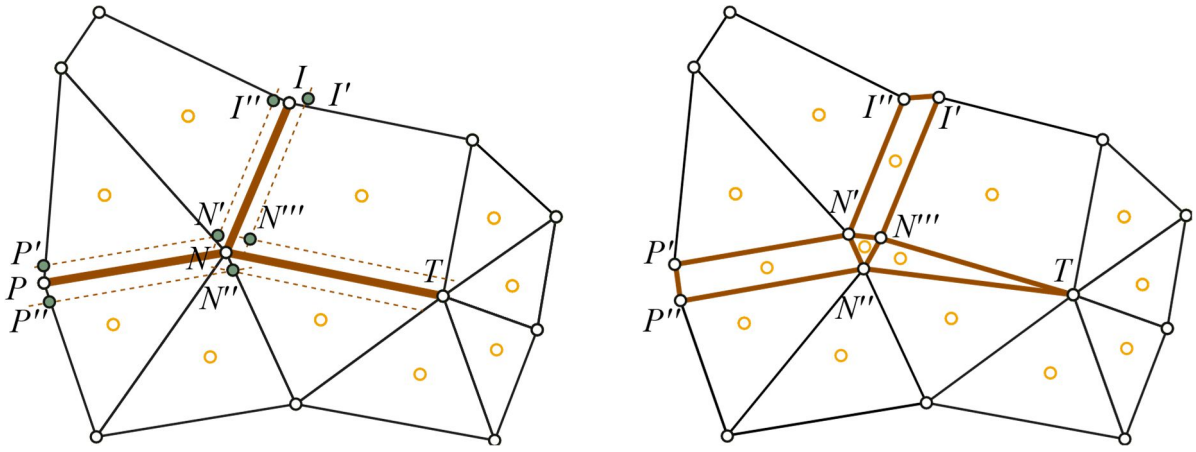

(a) (b)

Source: Author.

This strategy makes easier the management of the weighting associated to the node function values calculation (that is necessary for some cell-centered formulations), if compared, for example, with other methods that do not expand the fractures and solve their equations in a lower-dimensional domain, as the lower-dimension fracture model (LDFM) (AHMED et al., 2015; BRUM, 2016).

Figure 9.a shows the local set for the interpolation of the fracture node *I* in LDFM, with the blue arrow indicating all the cells which are involved in the node value interpolation ($\hat{k}, \hat{f}_1, \hat{h}, \hat{s}, \hat{f}_2, \hat{r}$ and $\hat{g}$), for the calculation of the flux crossing, among other faces, *IM* and *IL*. But if the fractures separating $\hat{k}$, $\hat{g}$ and $\hat{r}$ from $\hat{s}$ and $\hat{h}$ are, for example, barriers, there would be a function discontinuity through the fractures and the value of it on $\hat{k}$, $\hat{g}$ and $\hat{r}$ should not influence the flux calculation on *IL*. So, it would be necessary to evaluate for each edge sharing *I*, which cells would be the ones to participate in the interpolation. If the fracture is expanded (Figure 9.b), the node *I* becomes *I'* and *I''*, forming the edges *I'L* and *I''M*, each one with an appropriate set of cells to participate on its interpolation (see the blue arrows in Figure 9.b), without the necessity to determine in which edge is going to be the flux calculation.

Figure 9 – Set of grid cells for node interpolation. (a) In LDFM. (b) In HyG.

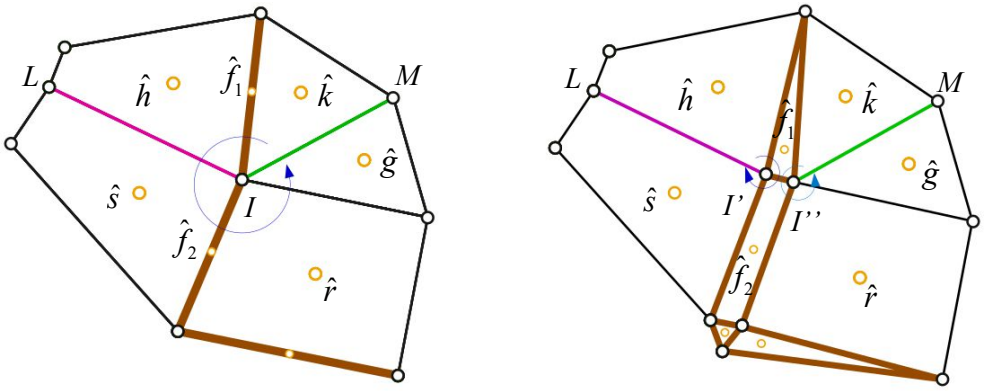

(a) (b)

Source: Author.

Other important advantage of the HyG is that it is possible to take full advantage of the full-pressure support (FPS) methods such as the MPFA-D, because it is possible to build

support regions including the expanded fractures (Figure 10.a). Therefore, it is possible to impose the flux continuity on the virtual edges between $\hat{k}$ and $\hat{f}_1$, and $\hat{h}$ and $\hat{f}_1$.

In LDFM (Figure 10.b) the calculation of the flux from $\hat{k}$ to $\hat{f}_1$ or from $\hat{h}$ to $\hat{f}_1$ is made by using triangle support regions, excluding the fracture information, that is why, in these cases, it is necessary to write an additional equation only for the fracture. The LDFM could leads to underutilization of the potential of the FPS methods.

Other advantage of the HyG relating to the LDFM is that, in the last one, the permeability tensor in a fracture is always assumed to be K-orthogonal (aligned with the fracture), but the HyG does not present this restriction.

Figure 10 – Support regions to the flux calculation. (a) In HyG. (b) In LDFM.

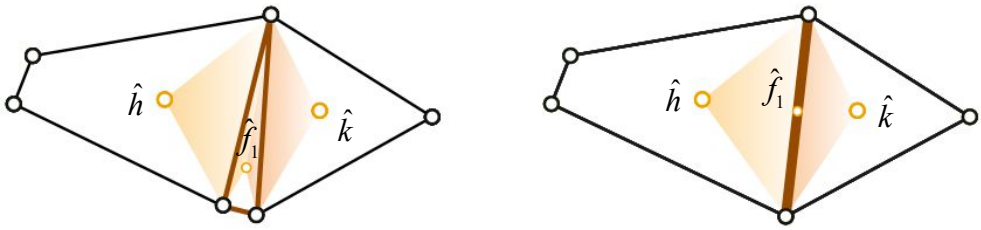

(a) (b)

Source: Author.

4 RESULTS

In this section, the results of the application of the MPFA-D in the context of HyG for the simulation of one-phase and two-phase flows in naturally fractured reservoirs are presented. First, a convergence test is shown, comparing the MPFA-D/HyG with CVD-MPFA/HyG (AHMED et al., 2017). Then, some results obtained by the MPFA-D/HyG for the simulation of single-phase flow are presented and compared with those obtained by the MPFA-O/HyG and with those obtained by the MPFA-D under the equidimensional strategy. Finally, some results obtained by the MPFA-D/HyG for the simulation of two-phase flow are presented and compared with other results found in literature. The simulations were performed using an Intel® Core™ i7-3770 3.40 GHz, with 7.89 GB of available RAM, with Windows 10 Pro© 64 bits and MATLAB® 2014a.

Unless otherwise indicated in the statement of the problem, the exponents n_w and n_o of Equation (2.2) are always equal to 2, the porosities are always set as 0.2 in the rock matrix and 1 in the fracture. In all examples in which IMPES scheme is used, the Courant number is 0.9, and in those in which SEQ is used, the nonlinear chosen tolerance δ is 10^{-3}. The rock matrix properties are referred to by the subscript *m* and the fracture properties are referred to by the subscript *f*.

4.1 One-phase flow in a reservoir with a central fracture

This problem was proposed by Sandve, Berre and Nordbotten (2012) and it was used to evaluate the convergence rates for pressure obtained with MPFA-D/HyG. It consists of a one-phase problem in a computational domain that contains a single fracture with the aperture *a* as shown in Figure 11. Dirichlet boundary conditions are imposed on all the boundaries of the domain according to the analytical solution, presented in the following equation:

$$p(x,y)=\begin{cases}\kappa\cos(x)\cosh(y)+(1-\kappa)\cos(x)\cosh(a/2); & (x,y)\in\Omega_m\\ \cos(x)\cosh(y); & (x,y)\in\Omega_f\end{cases} \tag{4.1}$$

In this case, permeability throughout the domain, including the fracture, is given by:

$$\underset{\sim}{K}(x,y)=\begin{cases}\underset{\sim}{K}_m(x,y); & (x,y)\in\Omega_m\\ \kappa\underset{\sim}{K}_m(x,y); & (x,y)\in\Omega_f\end{cases};\quad \underset{\sim}{K}_m=\begin{bmatrix}1 & 0\\ 0 & 1\end{bmatrix} \tag{4.2}$$

The distributed source term in defined as:

$$q=\begin{cases}(1-\kappa)\cos(x)\cosh(a/2); & (x,y)\in\Omega_m\\ 0; & (x,y)\in\Omega_f\end{cases} \tag{4.3}$$

The normalized error norms for pressure were defined by Sandve, Berre and Nordbotten (2012) as:

$$\|\varepsilon\|_{L2} = \frac{\sqrt{\sum_i V_i \left(p_i - \mathsf{p}_i\right)^2}}{\left[\max(\mathsf{p}) - \min(\mathsf{p})\right] \sum_i \Omega_i} \tag{4.4}$$

where p_i and p_i are respectively the numerical and analytical pressures calculated at the center and Ω_i is the volume (or area in 2-D) of the i-th cell of the mesh. This test was done for three fracture apertures a (10^{-3}, 10^{-4}, 10^{-5}) and, for each aperture, three values of the permeability contrast κ (10^{-4}, 1, 10^{4}) were used. The characteristic size of the grid cells is defined as:

$$L = \left(\frac{1}{n}\right) \sum_{i=1}^{n} \sqrt{\Omega_i} \tag{4.5}$$

where n is the number of cells in the mesh. The characteristic ratio of the mesh is defined as a/L. For the pressure variable, Figure 12 show convergence ratios of approximately 2 for all apertures and all permeability contrast values, such as the same errors magnitude in all cases.

Figure 11 – Computational domain for the one-phase flow problem in a reservoir with a central fracture.

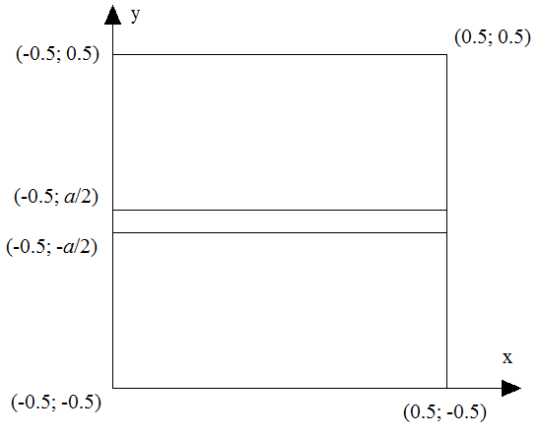

Source: Author.

The results of the MPFA-D were compared to those of the CVD-MPFA (also coupled with the hybrid-grid method) presented by Ahmed et al. (2017). These authors presented their results for two different versions of this formulation, the triangle-pressure support and the full-pressure support.

Figure 12 – One-phase flow in a reservoir with a central fracture. Normalized error versus characteristic size ratio with different values of permeability and aperture. The continuous lines are the results of the MPFA-D, the broken lines and the discrete marks (triangle, circle and asterisk) are, respectively, the results of the FPS and TPS CVD-MPFA (AHMED et al., 2017).

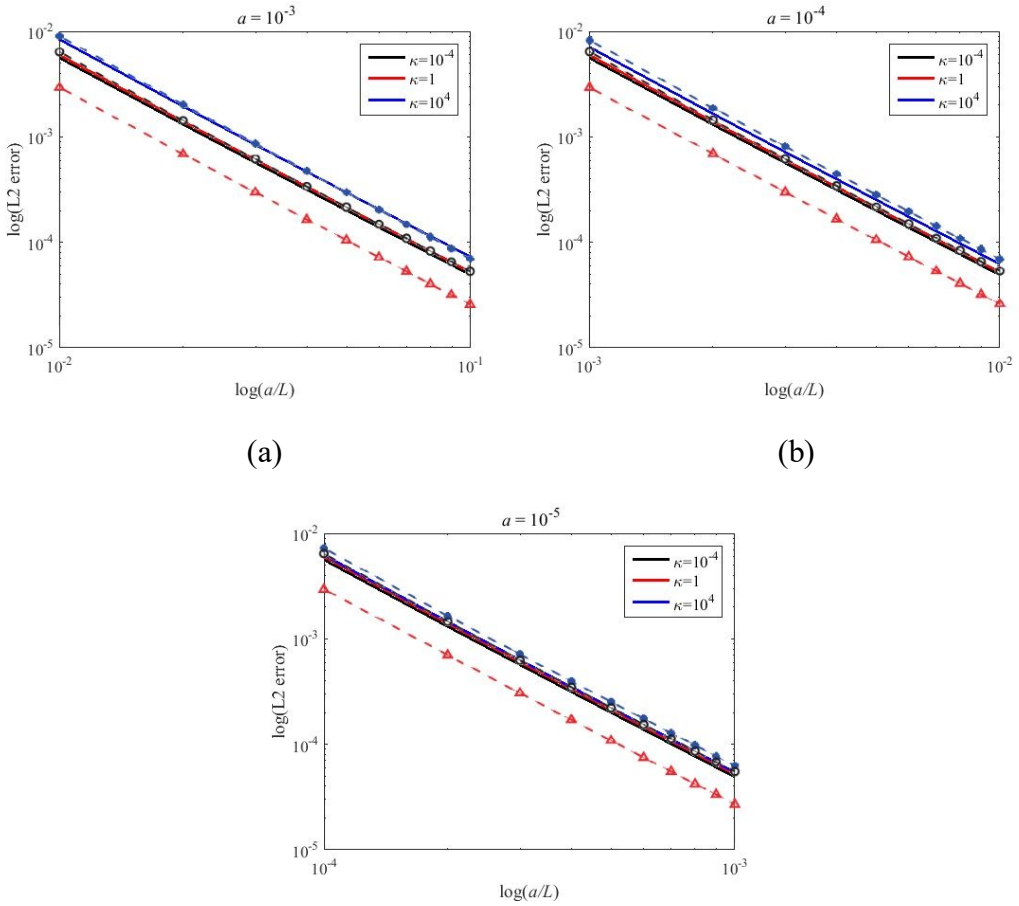

(a) (b)

(c)

Source: Author.

Our convergence ratios and errors magnitude are very close to those obtained by the CVD-MPFA (AHMED et al., 2017), as shown in Figure 12, despite the errors magnitude, for $\kappa = 1$, of both CVD-MPFA being slightly lower than those of the MPFA-D. Otherwise, for the other values of κ (for all values of a) the errors magnitude obtained by the MPFA-D are basically the same than those of the CVD-MPFA (Figure 12).

4.2 The ¼ five spot one-phase flow with multiple connected fractures

In this example, based on the work of Ahmed et al. (2017), the MPFA-D and the MPFA-O were applied, coupled with HyG, to solve a problem with multiple connected fractures, in which three permeability tensors were applied, with increasing anisotropy. The domain is defined as $\Omega = [0,1]\times[0,1]$m, discretized by 3,324 triangle cells, as shown in Figure 13, in which the bold lines indicate the fracture positions.

Figure 13 – Computational mesh for ¼ five spot one-phase flow with multiple connected fractures.

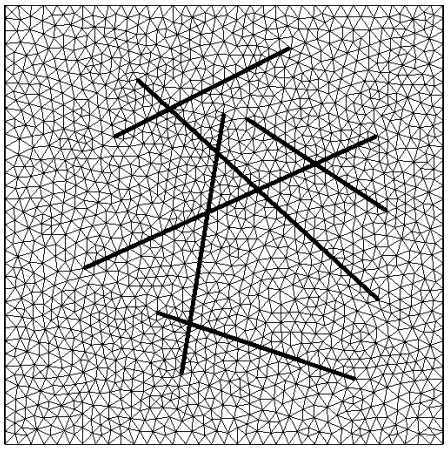

Source: Author.

The aperture is set as $a = 10^{-3}$ m for all the fractures. In the injection well, on the point $\vec{x}_I = (0;0)$m, the pressure is set as $p_I = 1$ bar and, in the production well, on the point $\vec{x}_P = (1;1)$m, the pressure is set as $p_P = 0$. There is no flow crossing the boundaries. The three tested permeability tensors for the rock matrix are an isotropic one ($\underset{\sim}{K}_{m,1}$ is the identity matrix), a mild anisotropic one ($\underset{\sim}{K}_{m,2}$ has an anisotropy ratio of 10:1 at an angle of $30°$) and a strongly anisotropic one ($\underset{\sim}{K}_{m,3}$ has an anisotropy ratio of 3000:1 at an angle of $25°$), all of them in mD and the two last ones defined as:

$$\begin{aligned}\underset{\sim}{K}_{m,2} &= \begin{bmatrix}\cos\theta & -\sin\theta\\ \sin\theta & \cos\theta\end{bmatrix}\begin{bmatrix}1 & 0\\ 0 & 0.1\end{bmatrix}\begin{bmatrix}\cos\theta & \sin\theta\\ -\sin\theta & \cos\theta\end{bmatrix};\ \text{with } \theta = 30°\\ \underset{\sim}{K}_{m,3} &= \begin{bmatrix}\cos\theta & -\sin\theta\\ \sin\theta & \cos\theta\end{bmatrix}\begin{bmatrix}0.3 & 0\\ 0 & 10^{-4}\end{bmatrix}\begin{bmatrix}\cos\theta & \sin\theta\\ -\sin\theta & \cos\theta\end{bmatrix};\ \text{with } \theta = 25°\end{aligned} \tag{4.6}$$

The permeability in the fracture is:

$$\underset{\sim}{K}_f = 10^5 \underset{\sim}{K}_m \tag{4.7}$$

The Figure 14 shows the results of both formulations under the three tensors.

Figure 14 – Pressure fields (in bar) of ¼ five spot one-phase flow with multiple connected fractures in different configurations. The regions with pressure bigger than 1 are marked by white and those with pressure lower than zero are marked by black.

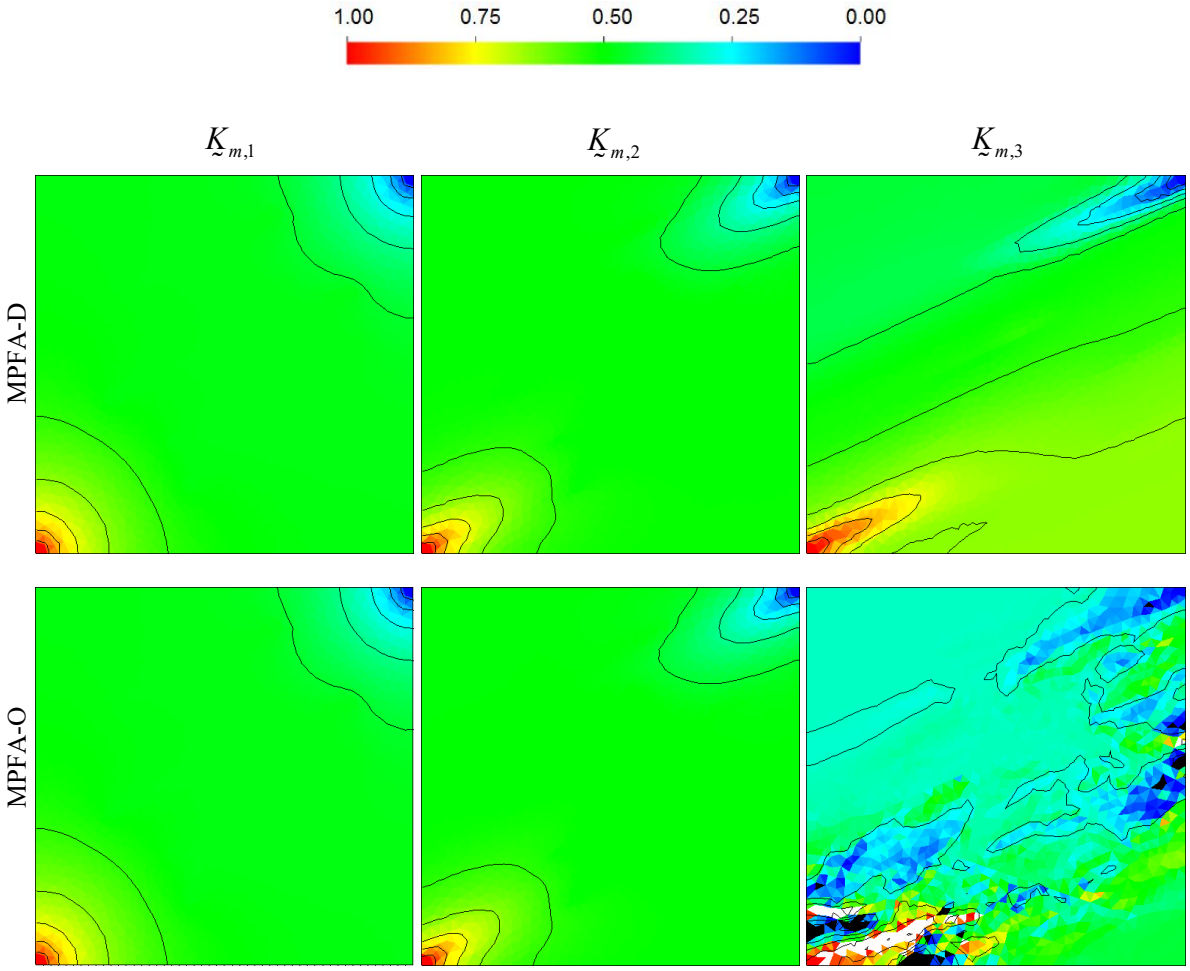

Source: Author.

Figure 14 shows that, under the isotropic ($\underset{\sim}{K}_{m,1}$) and the mild anisotropic ($\underset{\sim}{K}_{m,2}$) tensors, both formulations return the expected results. However, under the strongly anisotropic tensor ($\underset{\sim}{K}_{m,3}$), the MPFA-O, which is a triangle pressure support method, gives a wrong and oscillatory solution while the MPFA-D gives the expected solution.

Table 1 shows how the MPFA-O/HyG violates the discrete maximum and minimum principle in this case if used under a strongly anisotropic tensor.

Table 1 – Maximum and minimum pressures in bar from the ¼ five spot one-phase flow with multiple connected fractures.

	MPFA-D/HyG		MPFA-O/HyG	
	MAX	MIN	MAX	MIN
$\underset{\sim}{K}_{m,1}$	1	0	1	0
$\underset{\sim}{K}_{m,2}$	1	0	1	0
$\underset{\sim}{K}_{m,3}$	1	0	1.925	-1.674

Source: Author.

4.3 One-phase flow in a strongly anisotropic field and a diagonal fracture

In this example, based on the work of Gao and Wu (2013), the MPFA-D and the MPFA-O were applied, coupled with HyG, to solve a problem that involves a strongly anisotropic full-tensor field over a fractured domain defined as $\Omega = [0,1]\times[0,1]$m, discretized by 4,336 triangle cells, with a diagonal fracture (indicated as a bold line), as shown in Figure 15.a. The result of the MPFA-D on a mesh with the equidimensional representation of the fracture (the fracture represented as a 2-D entity), as shown in Figure 15.b and 15.c, was used as the reference result (this mesh has 537,276 triangle cells). The fracture aperture is $a = 10^{-4}$ m and the permeability tensor is:

$$\underset{\sim}{K} = \begin{bmatrix} \cos\theta & -\sin\theta \\ \sin\theta & \cos\theta \end{bmatrix} \begin{bmatrix} 1 & 0 \\ 0 & 10^{-4} \end{bmatrix} \begin{bmatrix} \cos\theta & \sin\theta \\ -\sin\theta & \cos\theta \end{bmatrix} \text{D; with } \theta = 40° \tag{4.8}$$

The Dirichlet boundary conditions (in bar) were set as follows:

$$g_D = \begin{cases} 1;\ [0,0.2]\times 0 \cup 0\times[0,0.2] \\ 0;\ [0.8,1]\times 1 \cup 1\times[0.8,1] \\ 0.5;\ [0.2,1]\times 0 \cup 0\times[0.2,1] \\ 0.5;\ [0,0.8]\times 1 \cup 1\times[0,0.8] \end{cases} \tag{4.9}$$

The permeability in the fracture is:

$$\underset{\sim}{K}_f = \kappa \underset{\sim}{K} \tag{4.10}$$

In this example, 3 values of κ (10^{-4}, 1, 10^{4}) were tested and the results are presented in Figure 16. This figure shows that the MPFA-D/HyG returns results that are comparable with those from the equidimensional strategy (the reference), showing to be capable to deal with this type of permeability tensor in all of the tested situations, including, in this example, respecting the maximum and minimum limits (see Table 2), which is neither guaranteed by this method. Otherwise, the MPFA-O, for example, which is just triangle pressure support, produces oscillatory wrong solutions in all tested cases.

The MPFA-D/HyG achieves satisfactory results and captures the effects of the fracture avoiding the refinement of the inside region of the fracture and the resulting over refinement of the region surrounding it. To solve this problem on the mesh shown in Figure 15.b took about 20 times longer than solve it on the mesh shown in Figure 15.a, using HyG. Table 2 shows the maximum and minimum pressures obtained by each strategy and how the MPFA-O/HyG violates the discrete maximum and minimum principle in all the tested cases.

Figure 15 – Computational mesh for one-phase flow in a strongly anisotropic field and a diagonal fracture. (a) Mesh to be used in the Hybrid-Grid Method. (b) Mesh to be used in equidimensional strategy. (c) Zoom in the mesh to be used in equidimensional strategy (15.b), highlighting the 2-D representation of the fracture.

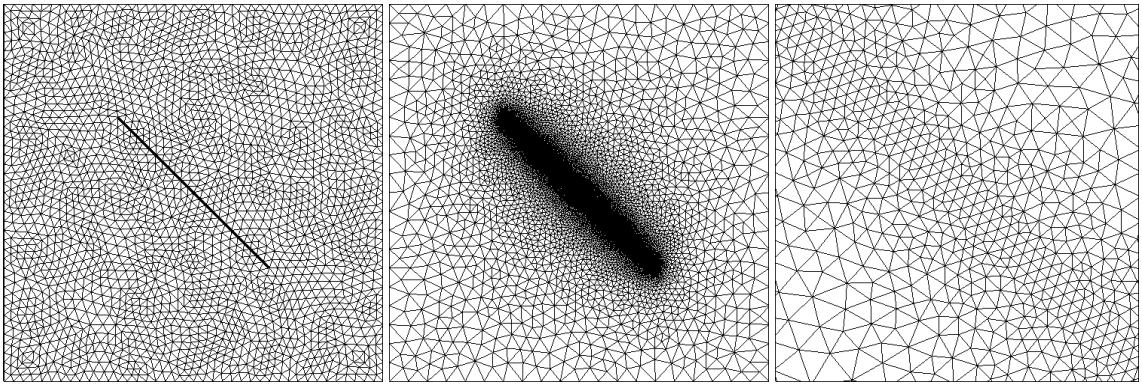

(a) (b) (c)

Source: Author.

Figure 16 – Pressure fields (in bar) of the one-phase flow problem on a strongly anisotropic field and a diagonal fracture in different configurations. The regions with pressure bigger than 1 are marked by white and those with pressure lower than zero are marked by black.

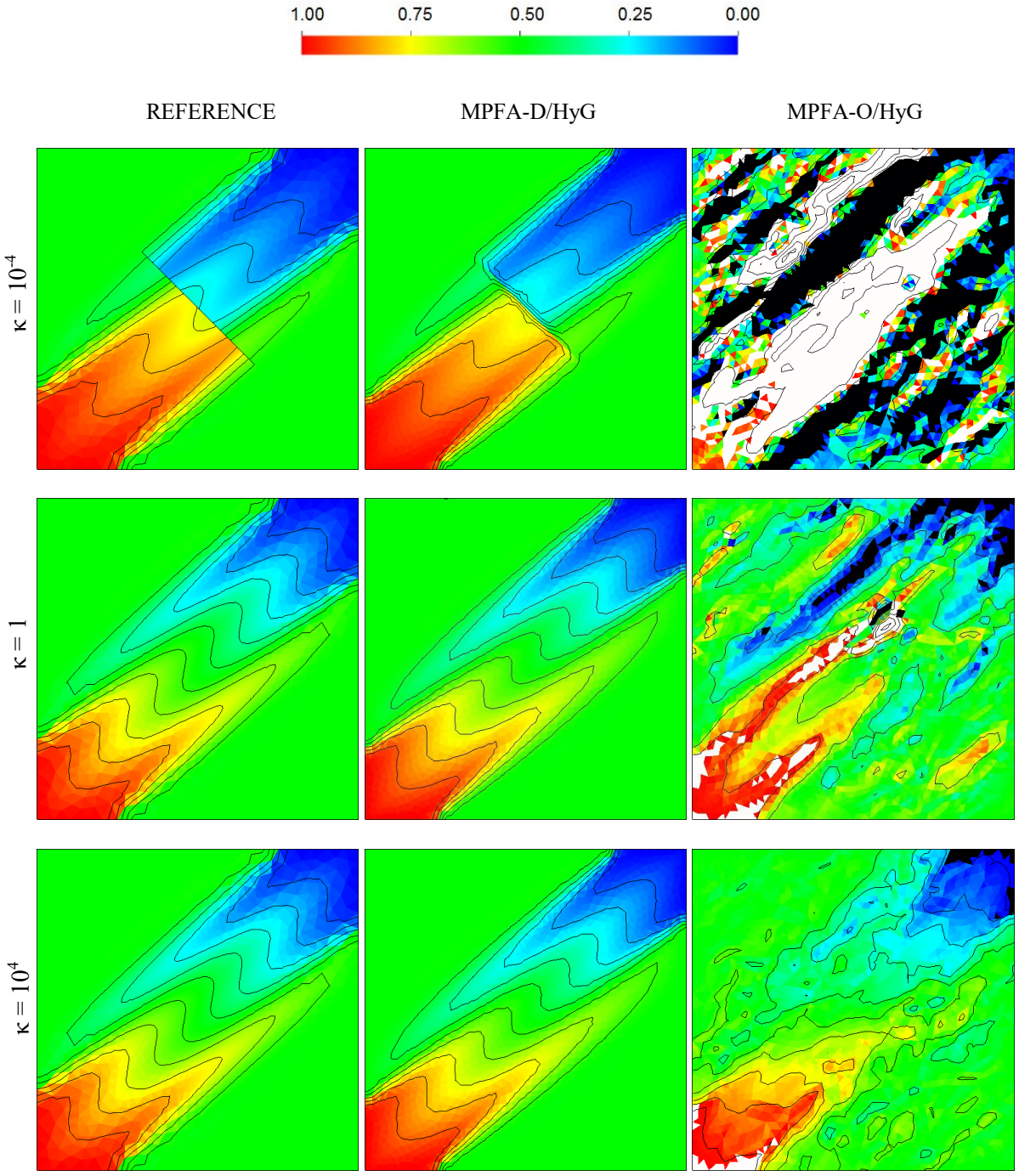

Source: Author.

Table 2 – Maximum and minimum pressures in bar from the one-phase flow problem on a strongly anisotropic field and a diagonal fracture.

	REFERENCE		MPFA-D/HyG		MPFA-O/HyG	
	MAX	MIN	MAX	MIN	MAX	MIN
$\kappa = 10^{-4}$	1	0	1	0	6.969	-5.168
$\kappa = 1$	1	0	1	0	1.921	-0.854
$\kappa = 10^{4}$	1	0	1	0	1.088	-0.098

Source: Author.

4.4 The ¼ five spot two-phase flow with a diagonal fracture

In this example, it was solved a two-phase flow problem presented by Brum (2016). The domain is defined as $\Omega = [0,1]\times[0,1]$, discretized by three meshes, as shown in Figure 17.a, 17.b and 17.c, respectively with 454, 944 and 1,910 triangle cells, with a diagonal fracture (marked as a bold line).

In the injection well, at the point $\vec{x}_P = (0;0)$, the pressure is set as $p_I = 1$ and, in the production well, at the point $\vec{x}_P = (1;1)$, the pressure is set as $p_P = 0$. There is no flow crossing the boundaries. The saturation is set as $\bar{S}_{w(I)} = 1$ on injection well and $\bar{S}_w^0 = 0$, initially, in the rest of the domain. The viscosities of water and oil are 1 and 0.45, respectively, and the permeability on the matrix is:

$$\underset{\sim}{K}_m = \begin{bmatrix} 2 & 1 \\ 1 & 2 \end{bmatrix} \tag{4.11}$$

The permeability in the fracture is $\underset{\sim}{K}_f = 10^4 \underset{\sim}{I}$, with $\underset{\sim}{I}$ being the identity matrix. The aperture of the fracture is $a_f = 10^{-3}$. The results presented by Brum (2016), obtained by using the MPFA-O coupled with the LDFM, were used as the reference to be compared with the results of the MPFA-D/HyG. For both formulations, the saturation equation was solved both implicitly (by using 4 as Courant number) and explicitly.

Figures 18 and 19 show the pressure fields on mesh 3, calculated by MPFA-D/HyG and MPFA-O/LDFM at 0.5 PVI and 1.0 PVI, respectively. The results are close to each other, but the first one seems to be more diffusive. Note that in the vicinity of the fracture, due to its

high permeability, the pressure is approximately constant, but in case of the MPFA-D/HyG this effect seems to be more prominent.

Figure 17 – Computational meshes for the ¼ five spot two-phase flow with a diagonal fracture. (a) Mesh 1. (b) Mesh 2. (c) Mesh 3.

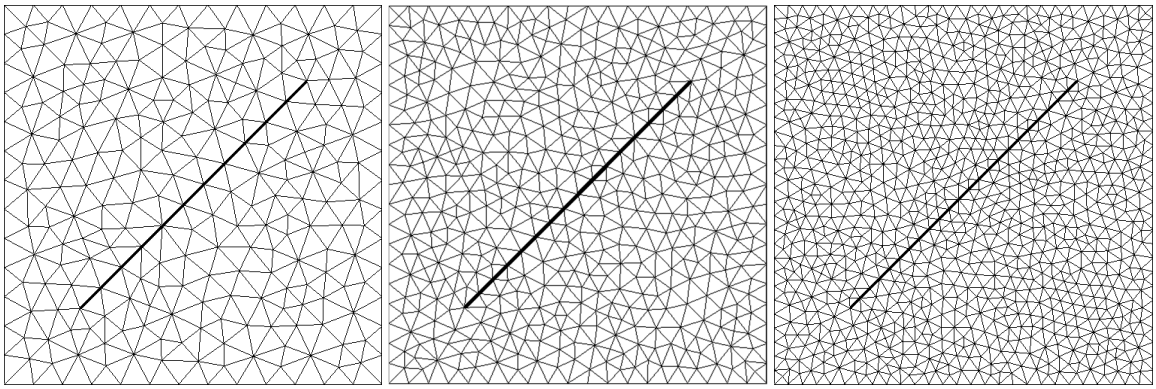

(a) (b) (c)

Source: Author.

Figures 20 and 21 show the saturation fields on the mesh 3, returned by the MPFA-D/HyG and MPFA-O/LDFM at 0.5 PVI and 1.0 PVI, respectively. Note that the fracture, because of its high permeability, conducts the injected water quickly to the lower pressure region. Comparing between the two formulations, the results are very close to each other, but it is possible to identify some qualitative differences. In the other hand, comparing IMPES and SEQ, under the same formulation, Figures 20 and 21 do not show appreciable discrepancies.

Figure 22 shows the production report obtained in this example. Note that the results obtained by the four strategies were very close to each other (Figure 22.a and Figure 22.b), but zooming in the graphs (Figure 22.c and Figure 22.d) it is possible to check the results of each strategy individually. Figure 22.c shows that the results of cumulative oil production of the MPFA-D/HyG and of the MPFA-O/LDFM do not vary significantly with the changing of the chosen scheme to solve the saturation equation.

Figure 18 – Pressure field for the ¼ five spot two-phase flow with a diagonal fracture at 0.5 PVI on Mesh 3.

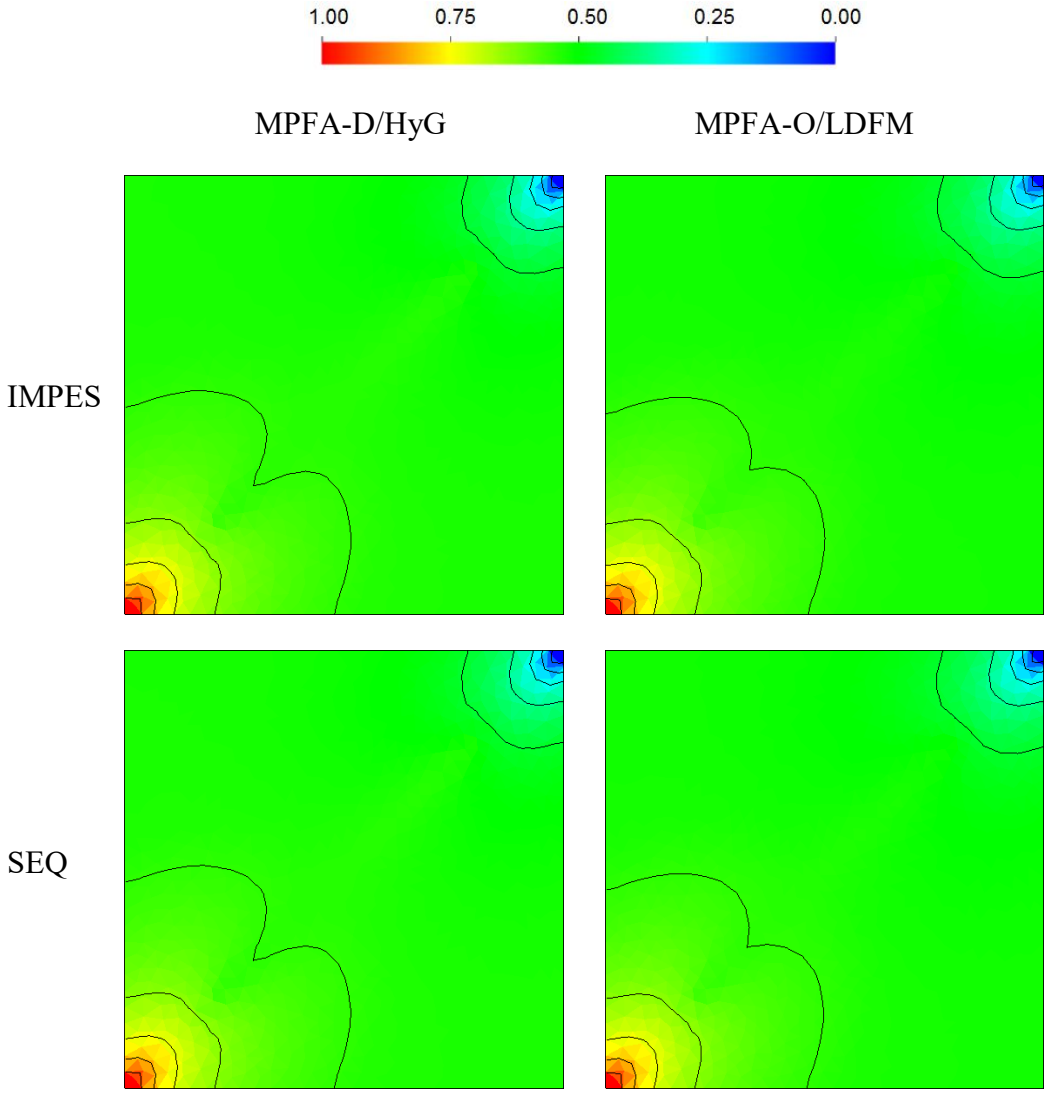

Source: Author.

Figure 22.c shows that the cumulative oil production calculated by the MPFA-O/LDFM is bigger than those from MPFA-D/HyG, no matter the used mesh. Figure 22.d shows that solving implicitly the saturation equation causes an anticipation of the water breakthrough for both MPFA-D/HyG and MPFA-O/LDFM, on the other hand, in each mesh the water breakthrough calculated by MPFA-D/HyG is never later than that from MPFA-O/LDFM.

Figure 19 – Pressure field for the ¼ five spot two-phase flow with a diagonal fracture at 1.0 PVI on Mesh 3.

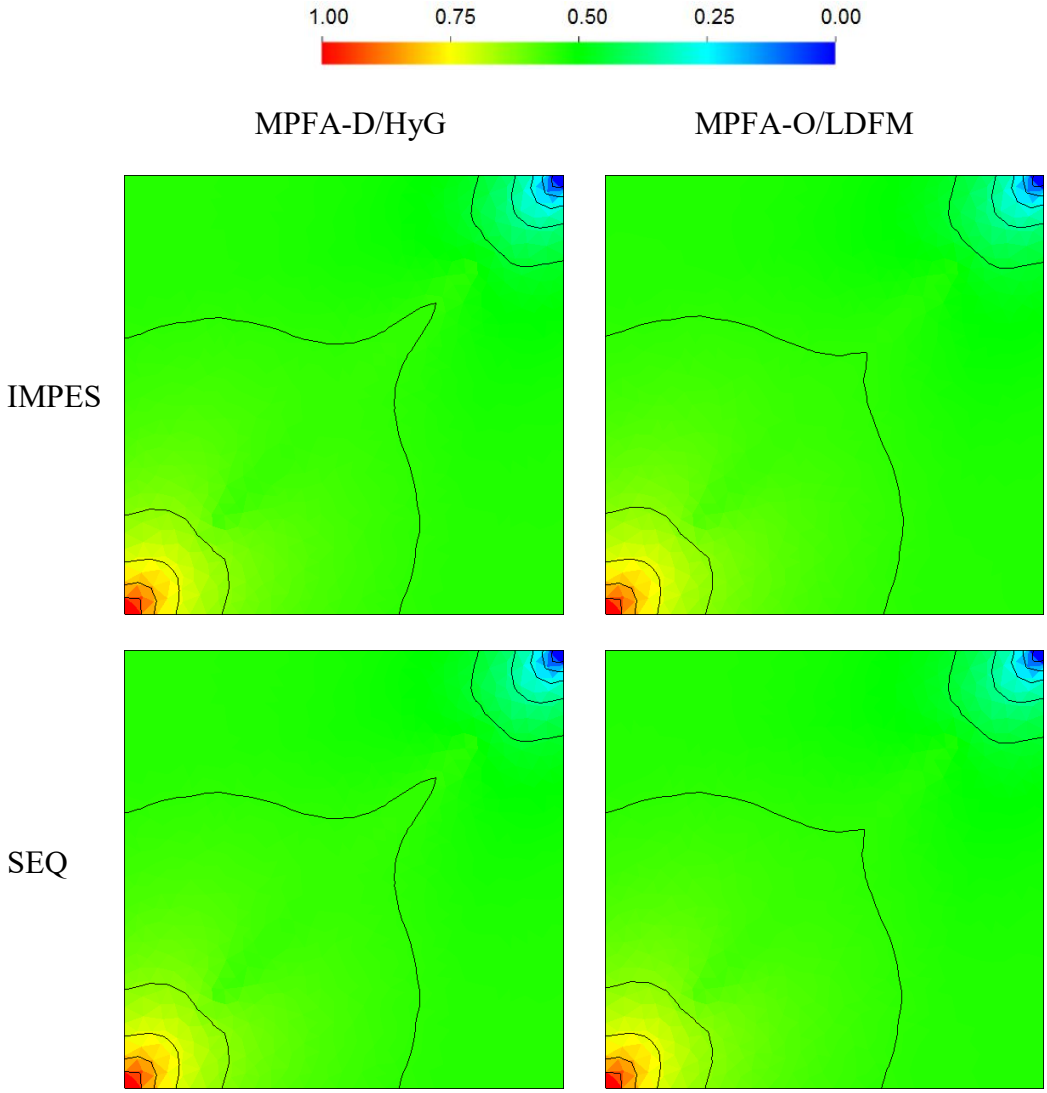

Source: Author.

Another thing to be noted in Figure 22.d is that the water breakthrough calculated by the MPFA-D/HyG on mesh 1 (the coarsest one) is considerably earlier than that calculated by the MPFA-O/LDFM, what curiously, in this case, leads the result of MPFA-D/HyG on mesh 1 to close to that one obtained on the mesh 3 (the most refined one). On meshes 2 and 3, the results of water breakthrough from both formulations are almost coincident.

Figure 20 – Saturation field for the ¼ five spot two-phase flow with a diagonal fracture at 0.5 PVI on Mesh 3.

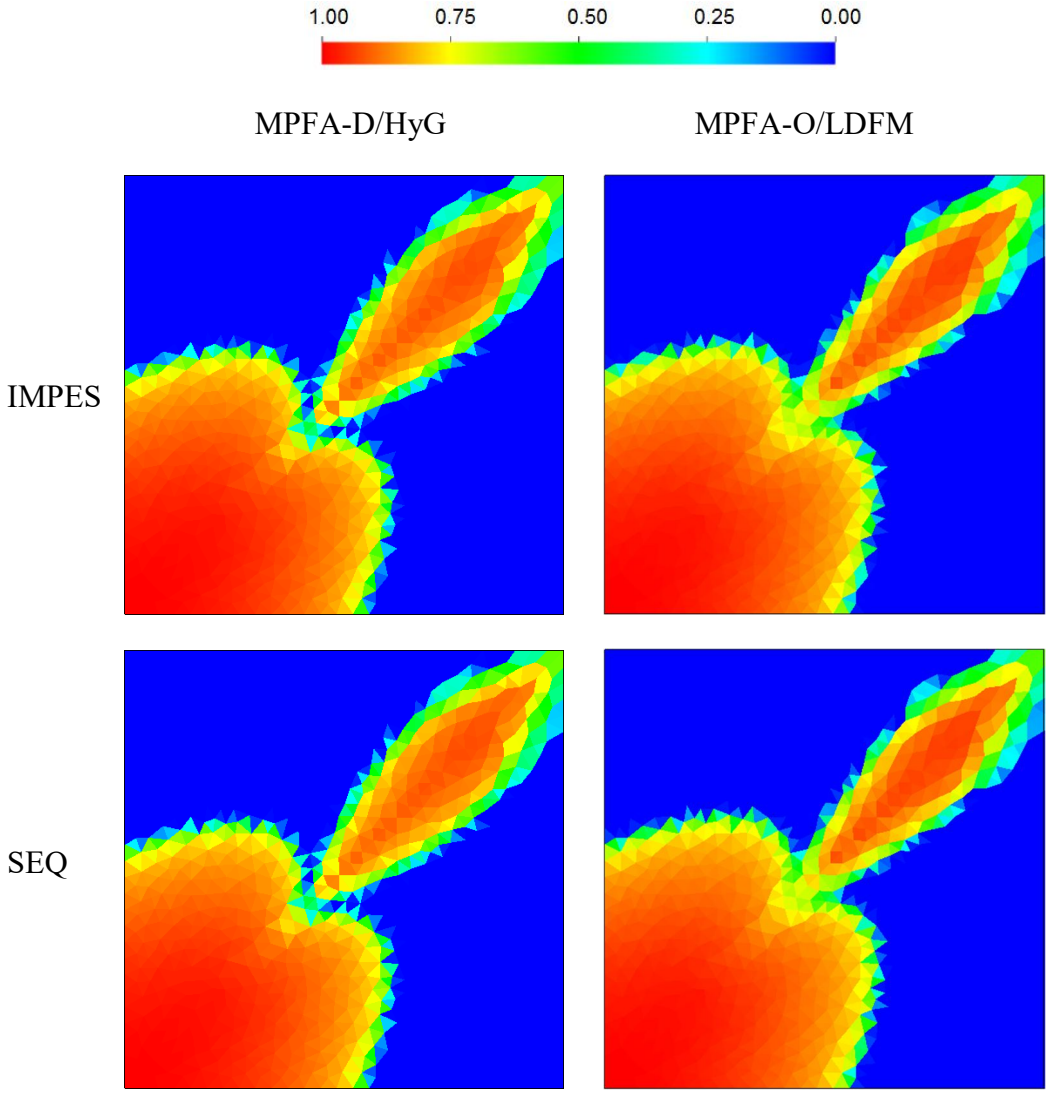

Source: Author.

Table 3 shows the simulation time of the two strategies, IMPES and SEQ, under MPFA-D/HyG, on the three meshes. In the performed tests, IMPES showed to be computationally costlier, with severe time step restrictions associated to it. The difference between IMPES and SEQ increased very significantly (in absolute terms) with the mesh refinement, although the relative difference between IMPES and SEQ (RDIS) underwent a very small reduction. The computational costs of both schemes, IMPES and SEQ, increased at similar rates with the mesh refinement.

Figure 21 – Saturation field for the ¼ five spot two-phase flow with a diagonal fracture at 1.0 PVI on Mesh 3.

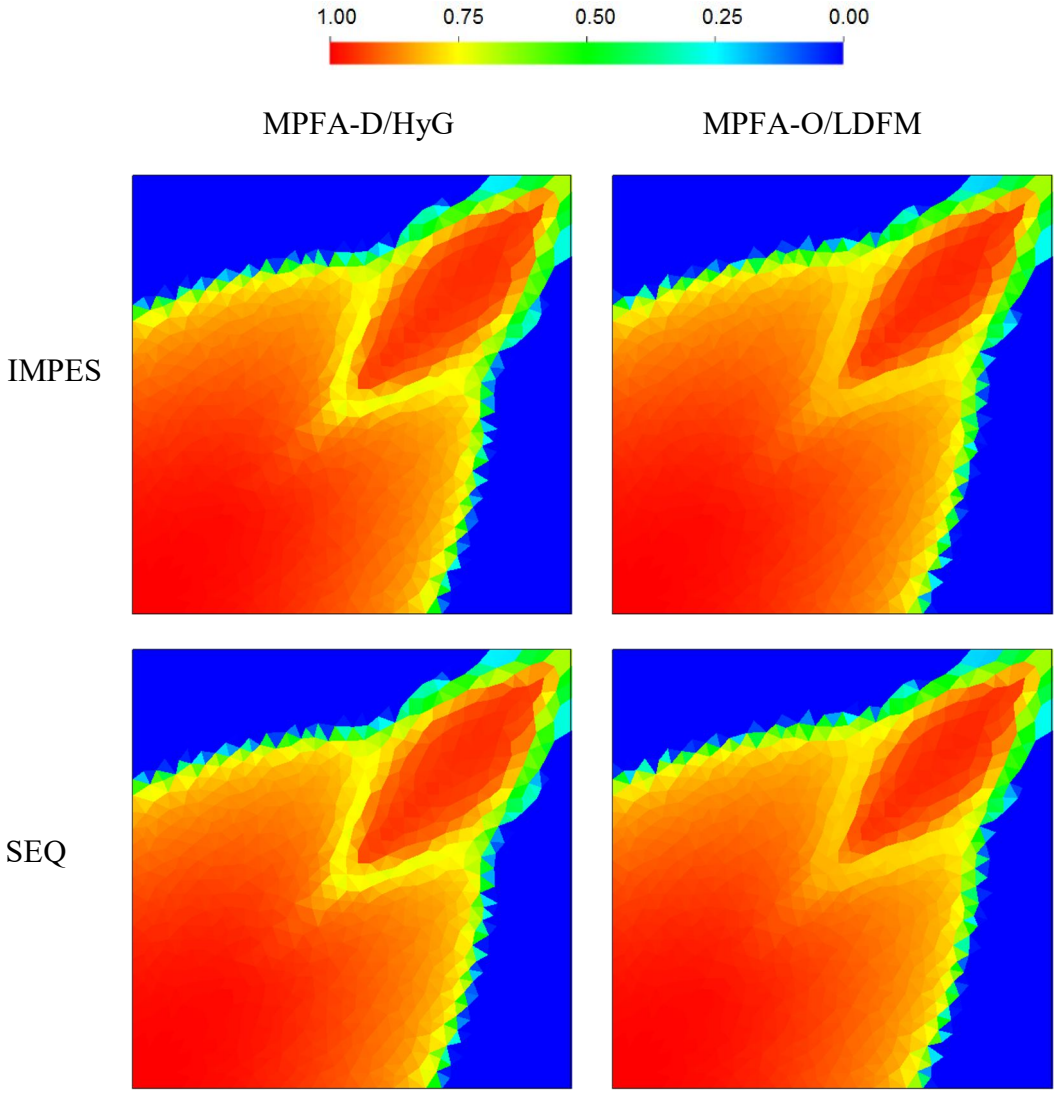

Source: Author.

Table 3 – Simulation time in seconds from the ¼ five spot two-phase flow with a diagonal fracture.

	SEQ	IMPES	RDIS
MESH 1	87	261	3
MESH 2	386	1099	2.85
MESH 3	2086	5260	2.52

Source: Author.

Figure 22 – Production report for the ¼ five spot two-phase flow with a diagonal fracture. (a) Cumulative Oil Production. (b) Watercut. (c) Zoom in the cumulative oil production graph. (d) Zoom in the watercut graph. (e) Legend.

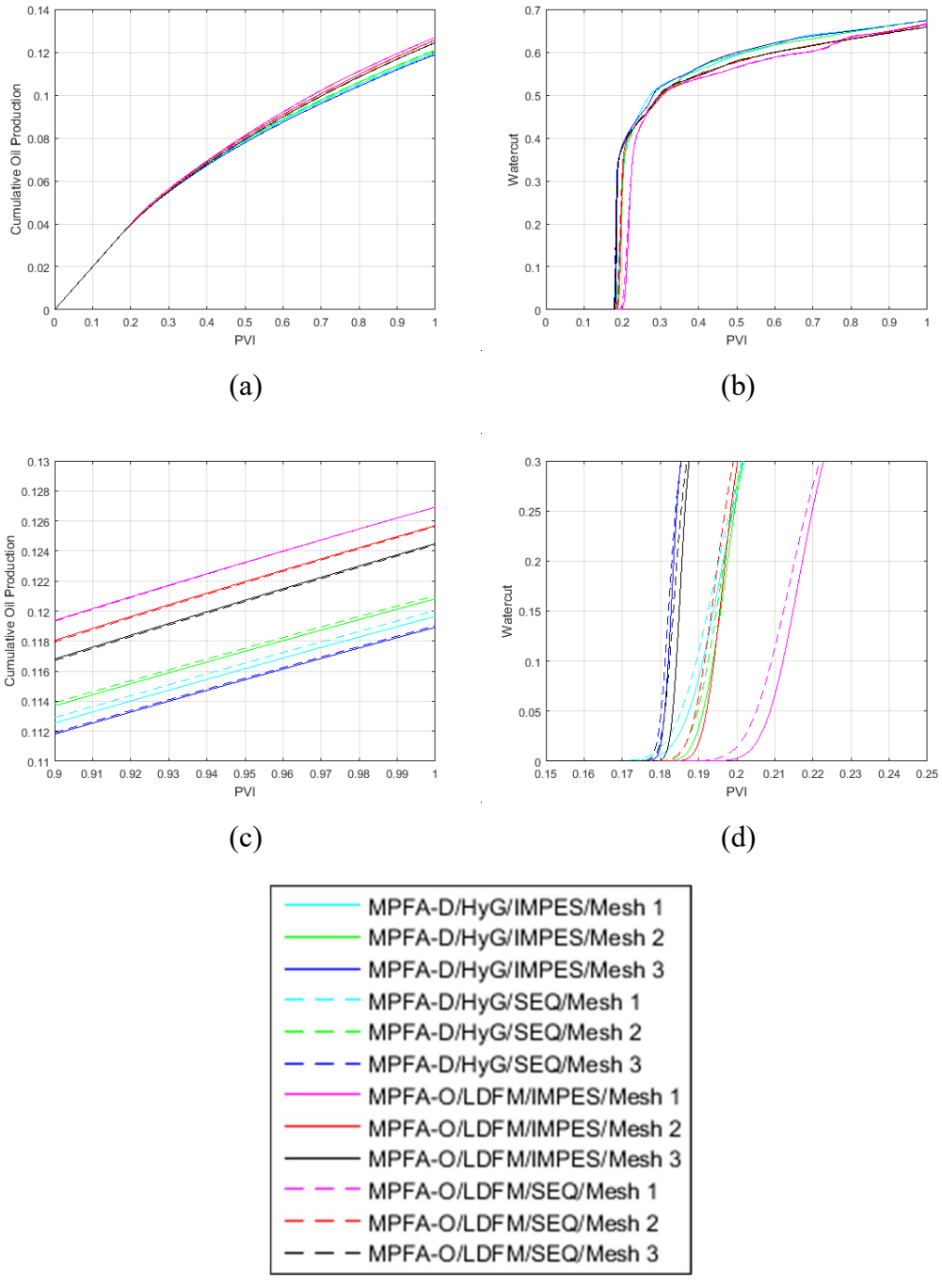

(a) (b) (c) (d) (e)

Source: Author.

4.5 The ¼ five spot two-phase flow with connected channel and barriers

In this example, a two-phase flow problem presented by Brum (2016) was solved. The domain is defined as $\Omega = [0,100]\times[0,100]$, with a diagonal channel (high permeability fracture) connected with barriers (low permeabilities fractures), as shown in Figure 23. In case 1, the channel does not cross the barriers, as shown in Figure 23.a. In case 2, the channel crosses through the barriers, as shown in Figure 23.b.

Figure 23 – Computational mesh for the ¼ five spot two-phase flow with connected channel (blue line) and barriers (red lines). (a) Case 1. (b) Case 2.

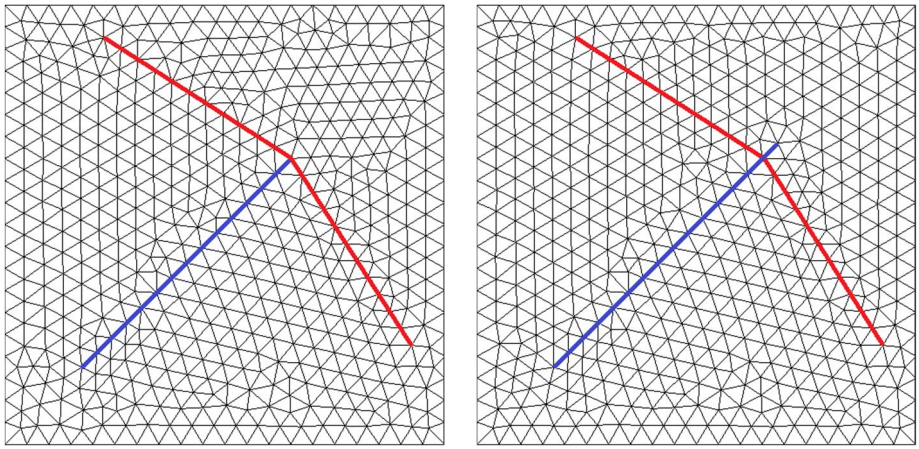

(a) (b)

Source: Author.

In the injection well, at the point $\vec{x}_P = (0;0)$, the pressure is set as $p_I = 1$ and, in the production well, at the point $\vec{x}_P = (100;100)$, the pressure is set as $p_P = 0$. There is no flow crossing the boundaries. The saturation is set as $\bar{S}_{w(I)} = 1$ on injection well and $\bar{S}_w^0 = 0$, initially, in the rest of the domain.

The viscosities of water and oil are set as 1, and the permeability on the matrix is:

$$\underset{\sim}{K}_m = \begin{bmatrix} 10^{-5} & 0 \\ 0 & 10^{-5} \end{bmatrix} \tag{4.12}$$

The permeability in the channel is $\underset{\sim}{K}_{f,1} = 8\cdot 10^{7}\underset{\sim}{K}_m$ and the permeability in the barriers is $\underset{\sim}{K}_{f,2} = 10^{-18}\underset{\sim}{K}_m$. The aperture of the fractures (channels and barriers) is $a_f = 10^{-4}$.

The results presented by Brum (2016), obtained by using the MPFA-O coupled with the LDFM, were used as the reference to be compared with the results of the MPFA-D/HyG. For both formulations, the saturation equation was solved only implicitly (by using 5 as Courant number), because of the hard time step restriction arising from the configuration of the problem.

Figures 24 and 25 show the pressure field, in both cases 1 and 2, calculated by the MPFA-D/HyG and MPFA-O/LDFM at 0.5 PVI and 1.0 PVI, respectively.

Figure 24 – Pressure field for the ¼ five spot two-phase flow with connected channel and barriers at 0.5 PVI.

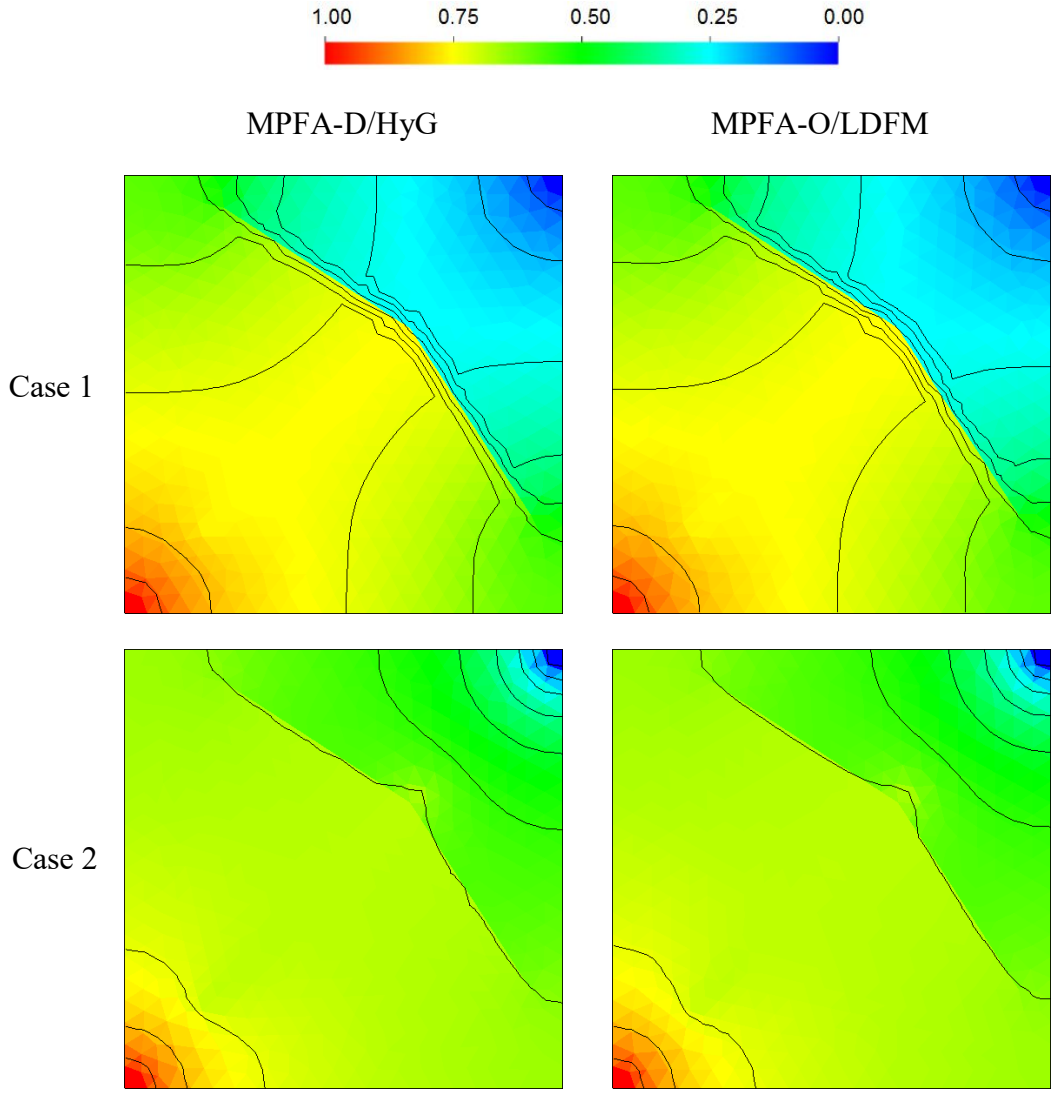

Source: Author.

Comparing the two formulations in each case (in Figures 24 and 25), the results are close to each other, so that it is not possible to identify relevant differences between the results of the two formulations. Note again that in the vicinity of the channel, due to its high permeability, the pressure is approximately constant.

Figure 25 – Pressure field for the ¼ five spot two-phase flow with connected channel and barriers at 1.0 PVI.

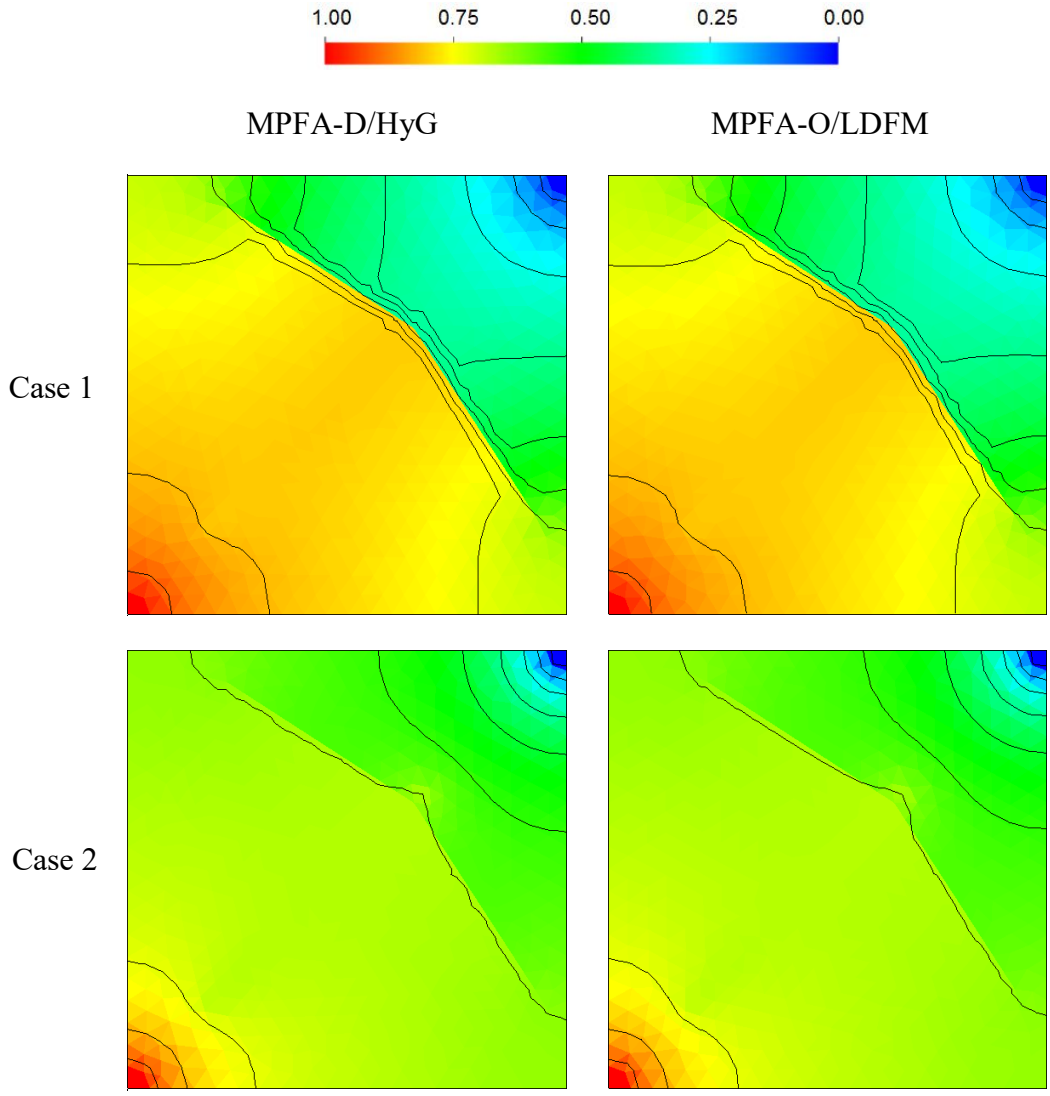

Source: Author.

Figures 26 and 27 show the saturation field returned by the MPFA-D/HyG and MPFA-O/LDFM at 0.5 PVI and 1.0 PVI, respectively. Note that in case 1, in which the channel does not cross the barrier, the water saturation front need to walk around the barriers

and, because of this, the water can sweep more oil from the reservoir, increasing the cumulative oil production, what can be seen in Figure 28.a. In case 2, the channel crosses through the barrier and conducts the injected water quickly to the production well, what causes an anticipation of the water breakthrough in relation to the case 1, what can be seen in Figure 28.b. Note that the results of cumulative oil production (Figure 28.a) and watercut (Figure 28.b) obtained in each case by the two formulations were very close to each other.

Figure 26 – Saturation field for the ¼ five spot two-phase flow with connected channel and barriers at 0.5 PVI.

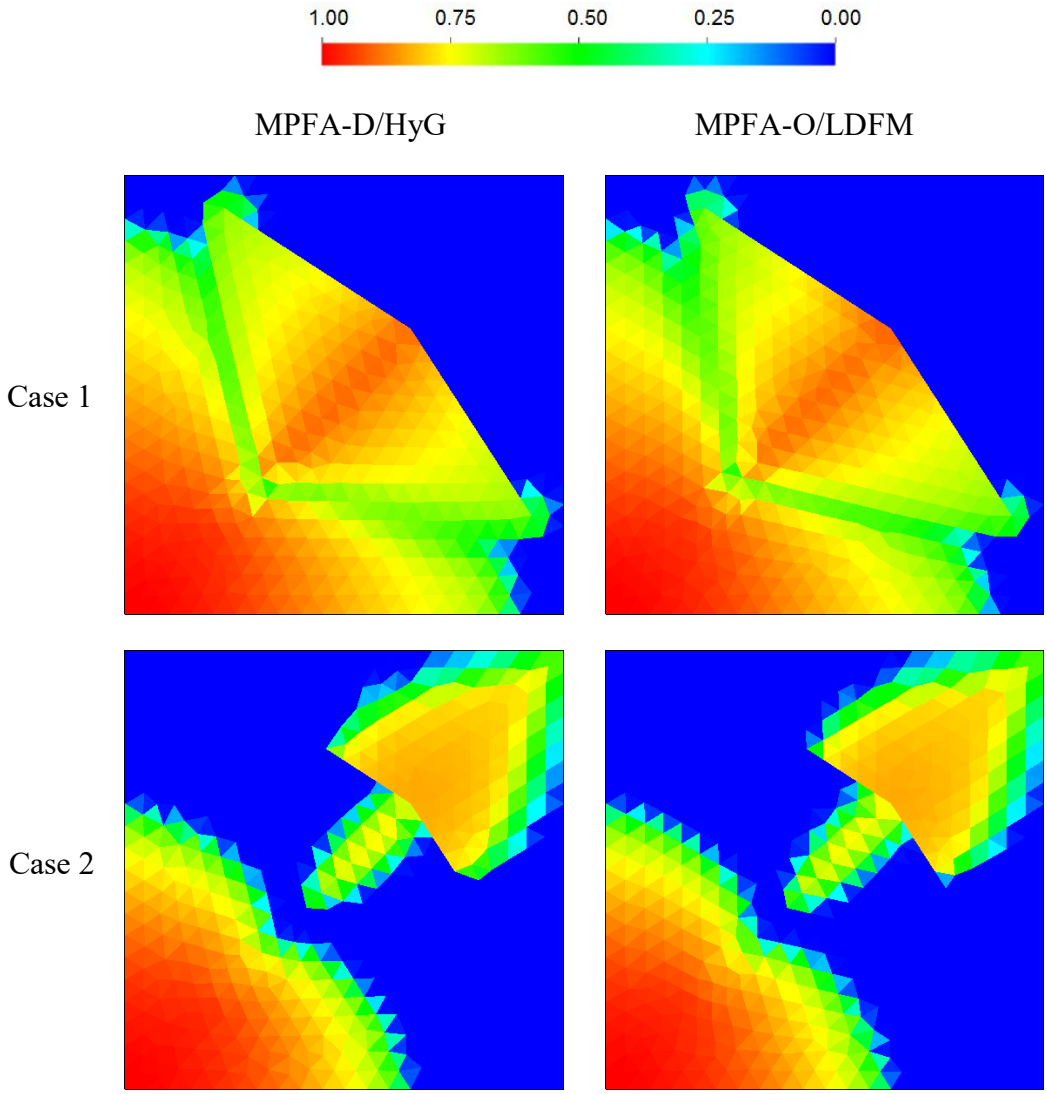

Source: Author.

Zooming in the graphs of cumulative oil production (Figure 28.c and Figure 28.d) and watercut (Figure 28.e and Figure 28.f) it is possible to verify the magnitude of the differences between the results of both formulations and note that they are always bigger in case 1 than in case 2.

Figure 27 – Saturation field for the ¼ five spot two-phase flow with connected channel and barriers at 1.0 PVI.

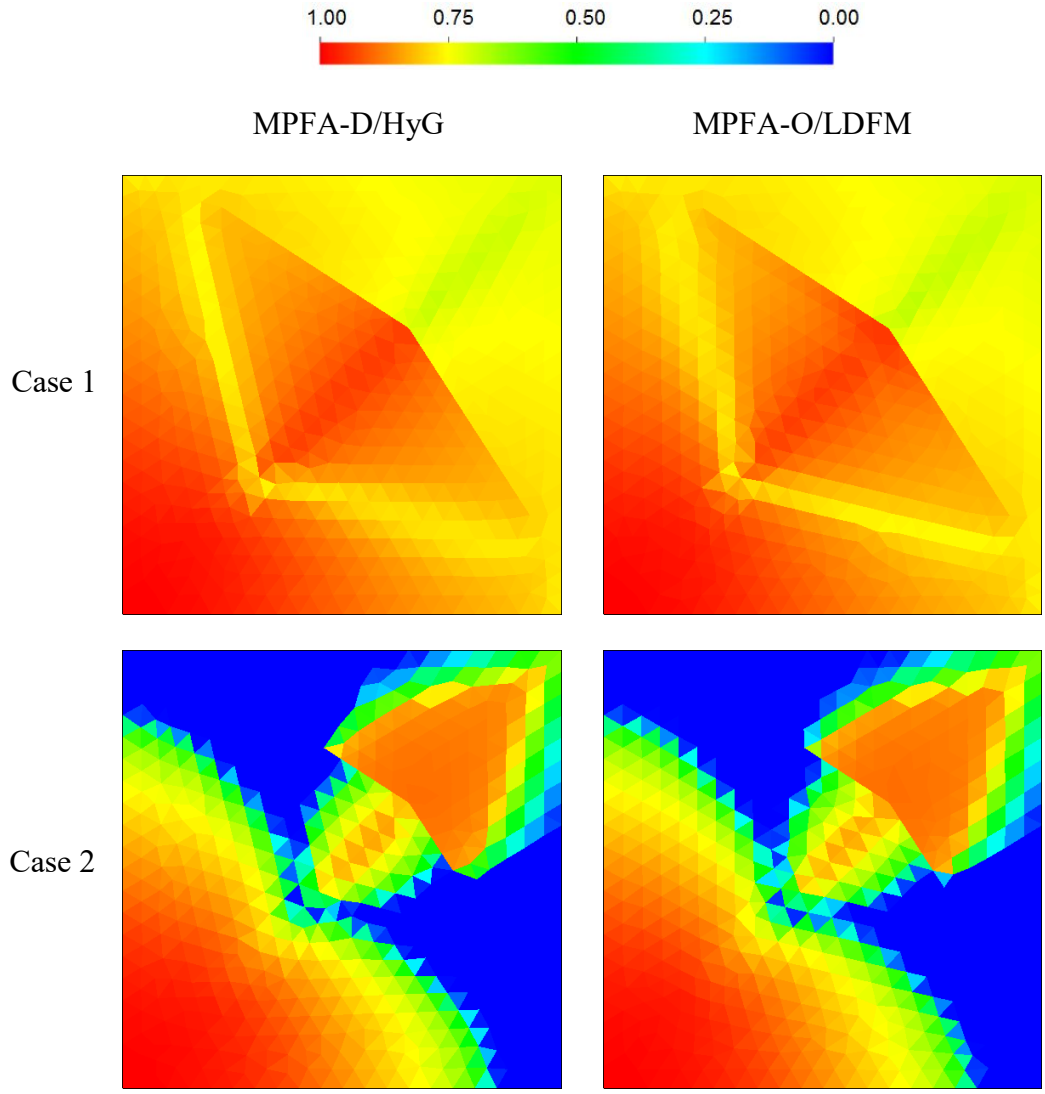

Source: Author.

4.6 The ¼ five spot two-phase flow with multiple connected fractures

In this example, MPFA-D/HyG was used to solve a two-phase flow problem in a domain defined as $\Omega = [0,1]\times[0,1]$m, with multiple connected fractures as shown in Figure 13,

with the bold lines indicating the fractures positions. In the injection well, at the point $\vec{x}_P = (0;0)$, water is injected with the rate of 0.1 PVI/year and, in the production well, at the point $\vec{x}_P = (1;1)$, the pressure is set as $p_P = 0$. There is no flow crossing the boundaries. The saturation equation was solved only implicitly (by using 5 as Courant number), because of the hard time step restriction arising from the configuration of the problem.

The saturation is set as $\bar{S}_{w(I)} = 1$ on injection well and $\bar{S}_w^0 = 0$, initially, in the rest of the domain. The viscosities of water and oil are set as 1 cP, and the rock matrix permeability tensors used in this example are $\underset{\sim}{K}_{m,2}$ and, defined in Equation (4.6). The fractures permeability tensors are:

$$\underset{\sim}{K}_a = 10^5 \underset{\sim}{K}_m;\ \underset{\sim}{K}_i = 10^5 \underset{\sim}{I} \tag{4.13}$$

Four cases were tested in this example: $\underset{\sim}{K}_{m,2}$ (mild anisotropic) and $\underset{\sim}{K}_{m,3}$ (strongly anisotropic), each one combined with $\underset{\sim}{K}_a$ (anisotropic) and $\underset{\sim}{K}_i$ (isotropic).

Figure 29 shows the pressure fields (with the scales in bar) after 1 year (0.1 PVI) for both tensors $\underset{\sim}{K}_{m,2}$ and $\underset{\sim}{K}_{m,3}$ (for the rock matrix) combined with the tensors $\underset{\sim}{K}_a$ and $\underset{\sim}{K}_i$ in the fractures. To illustrate how the presence of fractures modifies the pressure field, Figure 29 also shows how it would be, under the same permeability tensors, if fractures did not exist, which is easily obtained here only by "turning off" the hybrid-grid option, so that it is not built in the preprocessing of the method. First comparing the situations in which there are fractures with that in which they are "turned off", it can be noted that the presence of these fractures with high permeability in the central region of the domain creates therein a region of approximately constant pressure.

Comparing the cases with isotropic ($\underset{\sim}{K}_i$) and anisotropic ($\underset{\sim}{K}_a$) fracture permeability tensors, Figure 29 shows that under $\underset{\sim}{K}_{m,2}$ (the mild anisotropic tensor) there are no appreciable differences, otherwise under $\underset{\sim}{K}_{m,3}$ (the strongly anisotropic tensor), in addition to the visible qualitative differences, the pressures calculated in the injection well are also different (it is bigger in the case of the isotropic fracture).

Figure 30 shows the saturation fields after 1 year (0.1 PVI) for both tensors $\underset{\sim}{K}_{m,2}$ and $\underset{\sim}{K}_{m,3}$ (for the rock matrix) combined with the tensors $\underset{\sim}{K}_a$ and $\underset{\sim}{K}_i$ in the fractures.

Figure 28 – Production report for the ¼ five spot two-phase flow with connected channel and barriers. (a) Cumulative Oil Production. (b) Watercut. (c) Zoom in the cumulative oil production graph highlighting case 1. (d) Zoom in the cumulative oil production graph highlighting case 2. (e) Zoom in the watercut graph highlighting case 1. (f) Zoom in the watercut graph highlighting case 2.

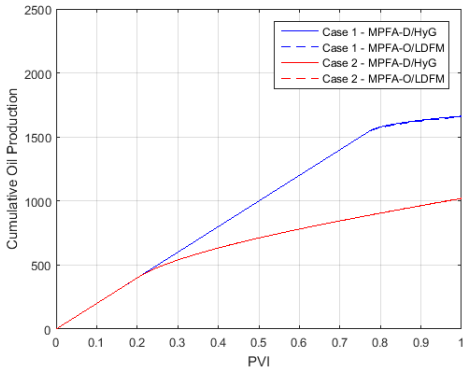

(a)

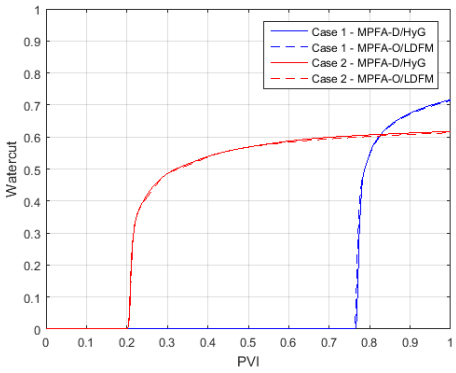

(b)

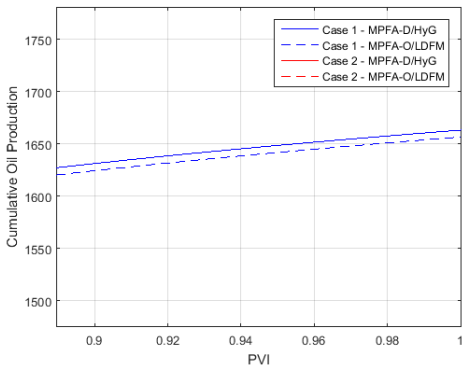

(c)

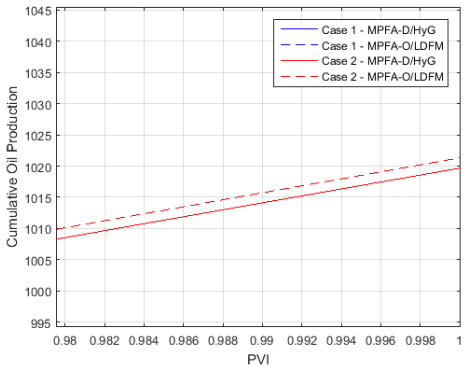

(d)

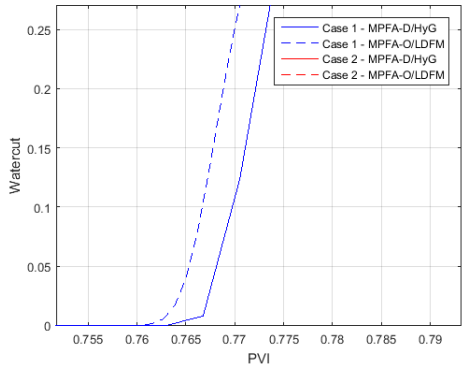

(e)

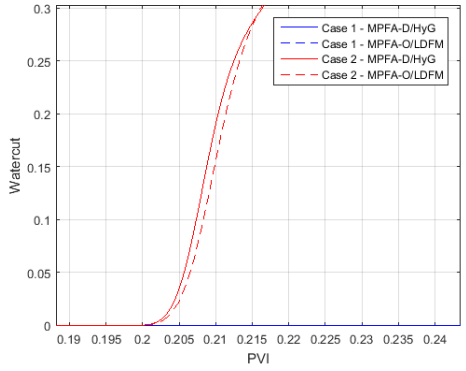

(f)

Source: Author.

Figure 29 – Pressure field (in bar) for the ¼ five spot two-phase flow with multiple connected fractures at 0.1 PVI (1 year).

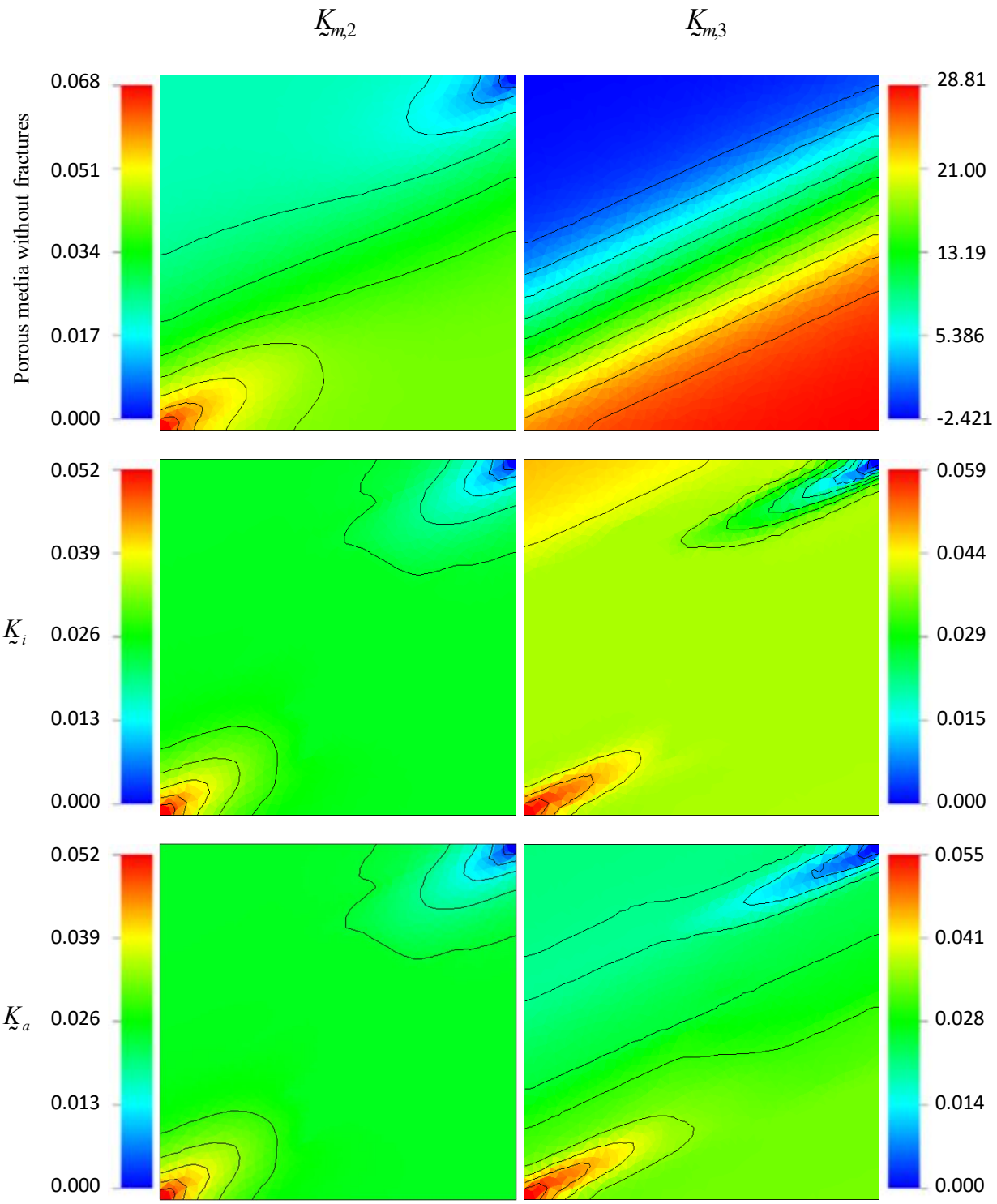

Source: Author.

Figure 30 – Saturation field for the ¼ five spot two-phase flow with multiple connected fractures at 0.1 PVI (1 year).

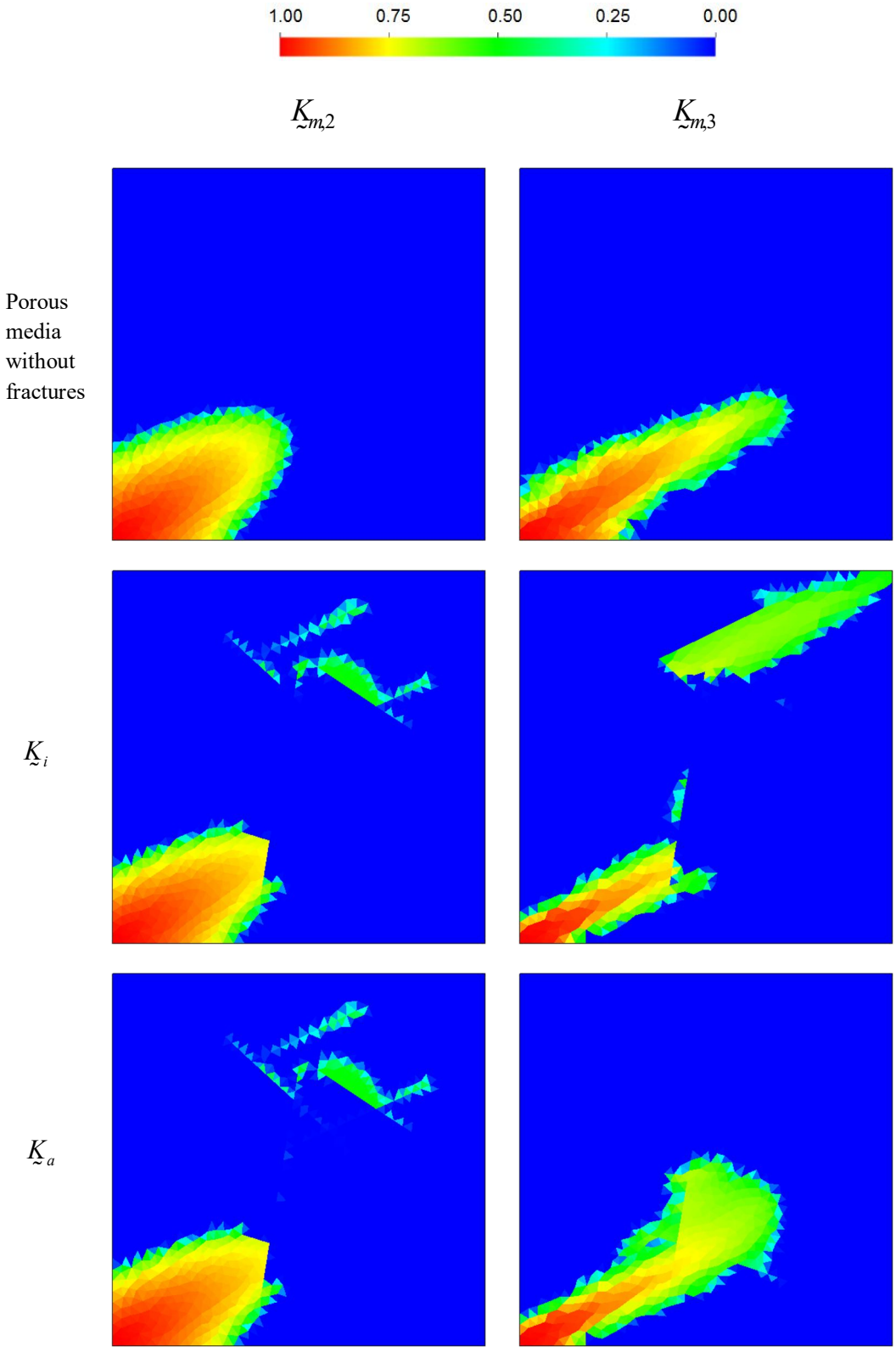

Source: Author.

To illustrate how the presence of fractures modifies the pressure field, Figure 30 also shows how it would be, under the same permeability tensors, if fractures did not exist. As expected, these high permeability fractures conduct the fluid to the lower pressure region more easily than the rock matrix. Under $\underset{\sim}{K}_{m,2}$ there are no appreciable differences between the results with $\underset{\sim}{K}_{a}$ and $\underset{\sim}{K}_{i}$, but under $\underset{\sim}{K}_{m,3}$ the application of the isotropic tensor in the fracture leads to the occurrence of the water breakthrough before 1 year, what do not occurs in the case in which the simulation is done considering the fracture permeability tensor as anisotropic as that one of the rock matrix, just multiplied by a constant. In this case, it is possible to note a huge difference between the applications of the isotropic and the anisotropic tensors inside the fracture. Differences that could even lead to completely different decisions in terms of reservoir management, indicating that one of these two options would be very wrong, that is why so important to have a formulation which is capable to deal with both.

5 CONCLUSIONS

This work presented a formulation for the numerical simulation of one and two-phase fluid flows in naturally fractured petroleum reservoirs. The formulation is based upon a Hybrid-Grid Method coupled with a non-orthodox Multipoint Flux Approximation finite volume method, with a Diamond Stencil (MPFA-D), to solve the elliptic pressure equation. The saturation equation was spatially discretized by the First Order Upwind Method (FOUM). Two schemes were used to couple the pressure and the saturation: IMPES (IMplicit Pressure and Explicit Saturation) and the SEQuential Implicit (SEQ). The latter showed to be particularly useful in this type of problems as the IMPES becomes extremely inefficient in some cases due to the severe time steps restriction. On the other hand, both returned very close results in the tested cases, with the SEQ just causing a negligible anticipation of the water breakthrough.

In order to evaluate the effectiveness and demonstrate the applicability of the proposed formulation (MPFA-D/HyG) to general permeability tensors on structured or unstructured grids, some examples of one-phase and two-phase flow problems found in literature were solved, using triangular and quadrilateral meshes.

In the convergence test, the proposed formulation performed very well when compared to the CVD-MPFA, a method that has been recently adapted in the Hybrid-Grid context (SANDVE; BERRE; NORDBOTTEN, 2012; AHMED et al., 2017), being capable of returning similar error magnitudes and equivalent convergence rates.

In one-phase flow tests, MPFA-D proved to be clearly superior to the classic MPFA-O, here also coupled with HyG, being capable to handle strongly anisotropic tensors even on a mesh distorted by the Hybrid-Grid strategy. In two-phase flow tests, the proposed formulation also performed well, presenting equivalent results to those obtained by more classical strategies, as the MPFA-O coupled with the LDFM (AHMED et al., 2015; BRUM, 2016).

As further works, the mesh preprocessing and the used data structure (which was originally made to deal with triangles and quadrilaterals) could be modified, so that they could handle any polygons, or at least hexagons, in order to avoid the creation by the HyG of those additional degrees of freedom at points of intersection of three or more fractures (as the triangle $N'N''N'''$ in Figure 8). The physics representation could also be improved, including capillarity, gravity and thermal effects, three-phase flows, etc., given that this is easier to do in models that represent the fractures explicitly as HyG. Besides, it would be interesting to study

the coupling of the HyG with a Non-Linear Finite Volume Method (NLFV) that honors the Discrete Maximum Principle (DMP) for general permeability tensors and unstructured polygonal meshes. Other suggested further works are to extend the MPFA-D/HyG to 3-D and incorporate it in a multiscale formulation, becoming it suitable to real field applications.

BIBLIOGRAPHY

AAVATSMARK, I. et al. Discretization on unstructured grids for inhomogeneous, anisotropic media. Part I. Derivation of the methods. *SIAM Journal on Scientific Computing*, v. 19, n. 5, p. 1700-1716, 1998. Cited 3 times on pages 19 and 37.

AAVATSMARK, I. et al. Discretization on unstructured grids for inhomogeneous, anisotropic media. Part II. Derivation of the methods. *SIAM Journal on Scientific Computing*, v. 19, n. 5, p. 1700-1716, 1998. Cited 3 times on pages 19 and 37.

AHMED, R. et al. CVD-MPFA full pressure support, coupled unstructured discrete fracture-matrix Darcy-flux approximations. *Journal of Computational Physics*, v. 349, p. 265-299, 2017. Cited 8 times on pages 18, 42, 46, 48, 49, 72.

AHMED, R. et al. Control-volume distributed multi-point flux approximation coupled with a lower-dimensional fracture model. *Journal of Computational Physics*, v. 284, p. 462–489, 2015. Cited 4 times on pages 18, 28, 44 and 71.

AZIZ, K.; SETTARI, A. *Petroleum Reservoir Simulation*, Applied Science Publishers LTD, 1979. Cited 3 times on pages 18, 27 and 34.

BACA, R.; ARNETT, R.; LANGFORD, D. Modeling fluid flow in fractured porous rock masses by finite element techniques. *Int. J. Numer. Methods Fluids*, v. 4, n. 4, p. 337–348, 1984. Cited 1 time on page 18.

BARENBLATT, G.; ZHELTOV, Y.; KOCHINA, I. Basic concepts in the theory of seepage of homogeneous fluids in fissured rocks. *PMM*, v. 24, n. 5, p. 852–864, 1960. Cited 2 times on page 16.

BEAR, J. *Dynamics of Fluids in Porous Media*. Elsevier, 1972. Cited 3 times on pages 24 and 25.

BERRE, I.; DOSTER, F.; KEILEGAVLEN, E. *Flow in fractured porous media: A review of conceptual models and discretization approaches*. Cornell University Library, 2018. Cited 5 times on pages 16 17 and 18.

BRUM, B. S. *Simulation of the Two-phase Flow of Water and Oil in Naturally Fractured Reservoirs Using Finite Volume Methods Coupled with Lower-Dimensional Fracture Models*. Master Thesis (In Portuguese), UFPE, 2016. Cited 7 times on pages 28, 44, 54, 61, 62 and 71.

BURDEN, R. L.; FAIRES, J. D. *Numerical Analysis*. Cengage Learning, 2010. Cited 1 time on page 42.

CARVALHO, D. K. *A Finite Volume Method Formulation with Data Structure by Edge for the Simulation of Fluid Flows in Porous Media*. PhD Thesis (In Portuguese), UFPE, 2005. Cited 4 times on page 19.

CARVALHO, D. K. et al. An unstructured edge-based finite volume formulation for solving immiscible two-phase flows in porous media. *Commun. Numer. Meth. Engng.*, v. 21, p. 747–756, 2005. Cited 2 times on page 26.

CHEN, Z.; HUAN, G.; MA, Y. *Computational Methods for Multiphase Flows in Porous Media*. SIAM, 2006. Cited 7 times on pages 15, 22, 25, 26 and 28.

CHEN, Q.; WAN, J.; YANG, Y.; MIFFLIN, R. T. Enriched Multi-Point Flux Approximation for General Grids. *Journal of Computational Physics*, v. 227, p. 1701–1721, 2008. Cited 1 time on page 38.

CONTRERAS, F. R. *A Cell-Centered Finite Volume Method for the Simulation of Two-phase Flows in Heterogeneous and Anisotropic Oil Reservoirs*. Master Thesis (In Portuguese). UFPE, 2012. Cited 1 time on page 19.

CONTRERAS, F. R. et al. A cell-centered multipoint flux approximation method with a diamond stencil coupled with a higher order finite volume method for the simulation of oil–water displacements in heterogeneous and anisotropic petroleum reservoirs. *Computers and Fluids*, v. 127, n. 1, p. 1–16, 2016. Cited 6 times on pages 25, 26, 27, 28, 30 and 34.

EDWARDS, M.; ROGERS, C. Finite volume discretization with imposed flux continuity for the general tensor pressure equation. *Comput. Geosci.*, v. 2, p. 259–290, 1998. Cited 4 times on pages 19, 23, 25 and 37.

EDWARDS, M.; ZHENG, H. A quasi-positive family of continuous Darcy-flux finite-volume schemes with full pressure support. *Journal of Computational Physics*, v. 227, p. 9333-9364, 2008. Cited 2 times on pages 19 and 38.

ERTEKIN, T.; ABOU-KASSEM, J. H.; KING, G. R. *Basic Applied Reservoir Simulation*. Society of Petroleum Engineers, 2001. Cited 3 times on pages 18, 21 and 22.

EWING, R. E. *The Mathematics of Reservoir Simulation*. SIAM, 1983. Cited 2 times on pages 15 and 24.

FANCHI, J. R. *Principles of Applied Reservoir Simulation*. Elsevier, 2005. Cited 1 time on page 23.

FLEMISCH, B.; FUMAGALLI, A.; SCOTTI, A. *A review of the XFEM-based approximation of flow in fractured porous media*. Politecnico di Milano, 2016. Cited 1 time on page 17.

FOX, R. W.; PRITCHARD, P. J.; MCDONALD, A. T. *Introduction to Fluid Mechanics*. In Portuguese. LTC, 2010. Cited 2 times on page 23.

FUMAGALLI, A.; SCOTTI, A. A numerical method for two-phase flow in fractured porous media with non-matching grids. *Advances in Water Resources*, v. 62, p. 454-464, 2013. Cited 1 time on page 17.

GAO, Z.; WU, J. A linearity-preserving cell-centered scheme for the heterogeneous and anisotropic diffusion equations on general meshes. *Int. J. Numer. Methods Fluids*, v. 67, p. 2157–2183, 2010. Cited 6 times on pages 19, 30, 33, 35 and 36.

GAO, Z.; WU, J. A small stencil and extremum-preserving scheme for anisotropic diffusion problems on arbitrary 2-D and 3-D meshes. *Journal of Computational Physics*, v. 250, p. 308–331, 2013. Cited 1 time on page 51.

GEIGER, S. et al. Combining Finite Element and Finite Volume for Efficient Multiphase Flow Simulations in Highly Heterogeneous and Structuraly Complex Geologic Media. *Geofluids*, v. 4, p. 284-299, 2004. Cited 1 time on page 19.

GEUZAINE, C.; REMACLE, J. F. Gmsh: a three-dimensional finite element mesh generator with built-in pre- and post-processing facilities. *International Journal for Numerical Methods in Engineering*, v. 79, n. 11, p. 1309-1331, 2009. Cited 1 time on page 28.

GHORAYEB, K.; FIROOZABADI, A. Numerical study of natural convection and diffusion in fractured porous media. *SPE Journal*, v. 5, n. 1, p. 12–20, 2000. Cited 1 time on page 17.

HE, C.; DURLOFSKY, L. J. Structured flow-based gridding and upscaling for modeling subsurface flow. *Advances in Water Resources*, v. 29, p. 1876-1892, 2006. Cited 1 time on page 19.

HIRSCH, C. *Numerical Computation of Internal and External Flows*. Wiley, 1994. Cited 2 times on pages 40 and 41.

HOTEIT, H.; FIROOZABADI, A. An efficient numerical model for incompressible two-phase flow in fractured media. *Advances in Water Resources*, v. 31, p. 891–905, 2008. Cited 4 times on pages 16, 18 and 28.

HURTADO, F. S. V. *An Element-Based Finite Volume Formulation for the Simulation of the Immersible Biphasic Displacement in Porous Medium.* Master Thesis (In Portuguese), UFSC, 2005. Cited 2 times on page 34.

KARIMI-FARD, M.; DURLOFSKY, L. J.; AZIZ, K. An efficient discrete-fracture model applicable for general-purpose reservoir simulators. *SPE Journal*, v. 9, n. 2, p. 227–236, 2004. Cited 2 times on pages 18 and 42.

KOZDON, J. E.; MALLISON, B. T.; GERRITSEN, M. G. Multidimensional upstream weighting for multiphase transport in porous media. *Comput. Geosci.*, v. 15, p. 399–419, 2011. Cited 3 times on pages 22 and 34.

LEE, S. H.; LOUGH, M. F.; JENSEN, C. L. Hierarchical modeling of flow in naturally fractured formations with multiple length scales. *Water Resources Research*, v. 37, n. 3, p. 443-455, 2001. Cited 1 time on page 18.

LI, L.; LEE, S. H. Efficient field-scale simulation of black oil in a naturally fractured reservoir through discrete fracture networks and homogenized media. *SPE Journal*, v. 11, n. 4, p. 750-758, 2008. Cited 1 time on page 17.

LONG, J. C. et al. Porous media equivalents for networks of discontinuous fractures. *Water Resources Research*, v. 18, n. 3, p. 645-658, 1982. Cited 1 time on page 16.

MANZOCCHI, T. et al. Fault transmissibility multipliers for flow simulation models. *Petroleum Geoscience*, v. 5, n. 1, p. 53–63, 1999. Cited 1 time on page 17.

MARTIN, V.; JAFFRÉ, J.; ROBERTS, J. E. Modelling fractures and barriers as interfaces for flow in porous media. *SIAM Journal on Scientific Computing*, v. 26, n. 5, p. 1667–1691, 2005. Cited 3 times on pages 16 and 18.

MATTHÄI, S. *Modelling multiphase flow in fractured porous rock*. Department of Earth Sciences and Engineering of the Imperial College London, 2005. Cited 1 time on page 15.

NILSEN, H. et al. Accurate Modelling of Faults by Multipoint, Mimetic, and Mixed Methods. *SPE Journal*, v. 17, n. 2, p. 568-579, 2012. Cited 2 times on page 17.

NOORISHAD, J.; MEHRAN, M. An upstream finite element method for solution of transient transport equation in fractured porous media. *Water Resources Research*, v. 18, n. 3, p. 588–596, 1982. Cited 1 time on page 18.

PEACEMAN, D. W. *Fundamentals of Numerical Reservoir Simulation*. Elsevier, 1977. Cited 6 times on pages 15, 18, 24, 25 and 26.

QUEIROZ, L. E. et al. On the accuracy of a nonlinear finite volume method for the solution of diffusion problems using different interpolations strategies. *International Journal for Numerical Methods in Fluids*, v. 74, n. 4, p. 270-291, 2014. Cited 1 time on page 34.

ROSA, A. J.; CARVALHO, R. S.; XAVIER, J. A. *Oil Reservoirs Engineering*. In Portuguese. Interciência, 2006. Cited 1 time on page 24.

SANDVE, T. H.; BERRE, I.; NORDBOTTEN, J. M. An efficient multi-point flux approximation method for discrete fracture-matrix simulations. *J. Comput. Phys.*, v. 231, n. 9, p. 3784–3800, 2012. Cited 6 times on pages 16, 18, 42, 46, 47, 71.

SCHWENCK, N. et al. Dimensionally reduced flow models in fractured porous media: crossings and boundaries. *Comput. Geosci.*, v. 19, n. 6, p. 1219–1230, 2015. Cited 1 time on page 17.

SOUZA, M. R. *Numerical Simulation of Two-phase Flow in Heterogeneous and Anisotropic Oil Reservoirs Using a "Truly" Multidimensional Finite Volume Method with High Order Approximation*. PhD Thesis (In Portuguese). UFPE, 2015. Cited 9 times on pages 19, 22, 28, 37 and 40.

SOUZA, M. R. et al. A Higher Resolution Flow Oriented Scheme with an Adaptive Correction Strategy for Distorted Meshes Coupled with a Robust MPFA-D Method for the Numerical Simulation of Two-Phase Flows in Heterogeneous and Anisotropic Petroleum Reservoirs. *Submitted to SPE Journal*, 2018. Cited 1 time on page 34.

TANNEHILL, J. C.; ANDERSON, D. A.; PLETCHER, R. H. *Computational Fluid Dynamis and Heat Transfer*. Taylor & Francis, 1997. Cited 1 time on page 39.

ULEBERG, K.; KLEPPE, J. *Dual porosity, dual permeability formulation for fractured reservoir simulation*. Trondheim RUTH Seminar, Norwegian University of Science and Technology, 1996. Cited 1 time on page 16.

WARREN, J.; ROOT, P. The behavior of naturally fractured reservoirs. *SPE Journal*, v. 3, n. 3, p. 245–255, 1963. Cited 1 time on page 16.

APPENDIX A – LPEW2 DERIVATION

Consider an inner vertex J whose pressure need to be interpolated. The first thing to do is to build a dual CV surrounding it. In the case of LPEW2, it is built connecting the midpoints of the edges sharing J. Imposing the divergence free (see Figure A1.a), the following expression is obtained:

$$\sum_{k=1}^{n_J} \vec{v}_{\bar{k}\,\overline{k+1}} \cdot \vec{N}_{\bar{k}\,\overline{k+1}} = 0 \tag{A.1}$$

Figure A1 - Sketch illustrating vertex pressure interpolation. (a) Divergence free imposition. (b) Flux continuity imposition on $J\bar{k}$.

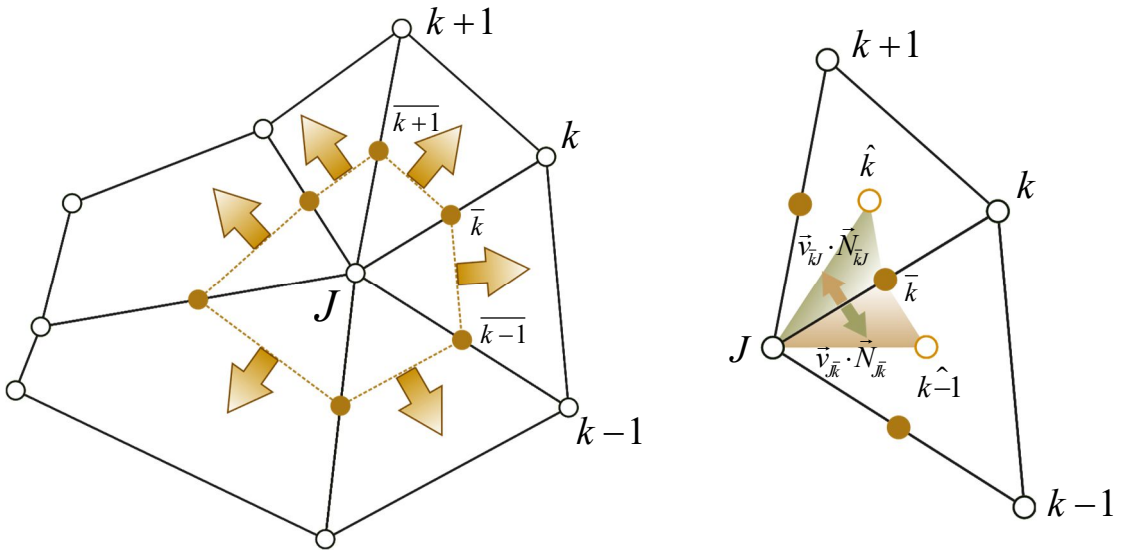

(a) (b)

Source: Author.

By the Lemma 1, the expressions for $\vec{v}_{\bar{k}\,\overline{k+1}} \cdot \vec{N}_{\bar{k}\,\overline{k+1}}$ can be written using the values of the pressures on $\bar{k}$, $\overline{k+1}$ and J as:

$$\vec{v}_{\bar{k}\,\overline{k+1}} \cdot \vec{N}_{\bar{k}\,\overline{k+1}} \simeq -\bar{T}_{\hat{k}}^{(n)} \left[\cot \vartheta_{\hat{k},2} \left(p_{\bar{k}} - p_J \right) + \cot \vartheta_{\hat{k},1} \left(p_{\overline{k+1}} - p_J \right) \right] - \bar{T}_{\hat{k}}^{(t)} \left(p_{\overline{k+1}} - p_{\bar{k}} \right) \tag{A.2}$$

where $\vartheta_{\hat{k},2} = \angle J\overline{k+1}\ \bar{k}$ and $\vartheta_{\hat{k},1} = \angle J\bar{k}\ \overline{k+1}$. Beyond this:

$$\bar{T}_{\hat{k}}^{(n)} = \lambda_{\hat{k}} \frac{\left(\vec{N}_{\overline{k\,k+1}}\right)^T \underset{\sim}{K}_{\hat{k}} \left(\vec{N}_{\overline{k\,k+1}}\right)}{\left|\overrightarrow{\overline{k\,k+1}}\right|^2};\ \bar{T}_{\hat{k}}^{(t)} = \lambda_{\hat{k}} \frac{\left(\vec{N}_{\overline{k\,k+1}}\right)^T \underset{\sim}{K}_{\hat{k}} \left(\overrightarrow{\overline{k\,k+1}}\right)}{\left|\overrightarrow{\overline{k\,k+1}}\right|^2}; \tag{A.3}$$

Rewriting Equation (A.2), the following expression is obtained:

$$\vec{v}_{\bar{k}\ \overline{k+1}} \cdot \vec{N}_{\bar{k}\ \overline{k+1}} \simeq \left(\bar{T}_{\hat{k}}^{(t)} - \bar{T}_{\hat{k}}^{(n)} \cot \vartheta_{\hat{k},2}\right)\left(p_{\bar{k}} - p_J\right) - \left(\bar{T}_{\hat{k}}^{(t)} + \bar{T}_{\hat{k}}^{(n)} \cot \vartheta_{\hat{k},1}\right)\left(p_{\overline{k+1}} - p_J\right) \tag{A.4}$$

Analogously:

$$\vec{v}_{\overline{k-1}\ \bar{k}} \cdot \vec{N}_{\overline{k-1}\ \bar{k}} \simeq \left(\bar{T}_{\hat{k-1}}^{(t)} - \bar{T}_{\hat{k-1}}^{(n)} \cot \vartheta_{\hat{k-1},2}\right)\left(p_{\overline{k-1}} - p_J\right) - \left(\bar{T}_{\hat{k-1}}^{(t)} + \bar{T}_{\hat{k-1}}^{(n)} \cot \vartheta_{\hat{k-1},1}\right)\left(p_{\bar{k}} - p_J\right) \tag{A.5}$$

Note that each term $\left(p_{\bar{k}} - p_J\right)$ will appear in two flow expressions and this is the reason why the Equation (A.1) can be rewritten in the following generalized form:

$$\sum_{k=1}^{n_J}\left(\bar{T}_{\hat{k-1}}^{(t)} - \bar{T}_{\hat{k}}^{(t)} + \bar{T}_{\hat{k-1}}^{(n)} \cot \vartheta_{\hat{k-1},1} + \bar{T}_{\hat{k}}^{(n)} \cot \vartheta_{\hat{k},2}\right)\left(p_{\bar{k}} - p_J\right) = 0 \tag{A.6}$$

Aiming to eliminate these auxiliary variables on the edges it is necessary to impose the flux continuity on the half edges $J\bar{k}$ (see Figure A1.b):

$$\vec{v}_{J\bar{k}} \cdot \vec{N}_{J\bar{k}} + \vec{v}_{\bar{k}J} \cdot \vec{N}_{\bar{k}J} = 0 \tag{A.7}$$

These flux expressions can be written, by Lemma 1, using the pressure values on $\bar{k}$, $\hat{k}$, $\hat{k+1}$ and J as:

$$\begin{aligned} &T_{\hat{k},1}^{(n)} \eta_{k,1}\left(p_{\hat{k}} - p_J\right) - \left(T_{\hat{k},1}^{(t)} + T_{\hat{k},1}^{(n)} \cot \theta_{\hat{k},1}\right)\left(p_{\bar{k}} - p_J\right) + \\ &+ T_{\hat{k-1},2}^{(n)} \eta_{k-1,2}\left(p_{\hat{k-1}} - p_J\right) + \left(T_{\hat{k-1},2}^{(t)} - T_{\hat{k-1},2}^{(n)} \cot \theta_{\hat{k-1},2}\right)\left(p_{\bar{k}} - p_J\right) = 0 \end{aligned} \tag{A.8}$$

where $\theta_{\hat{k},1} = \angle \bar{k} J \hat{k}$ and $\theta_{\hat{k-1},2} = \angle k\hat{-}1 J\bar{k}$. Beyond this:

$$\eta_{k,1} = \frac{\left|\overrightarrow{J\bar{k}}\right|}{h_{Jk}^{\hat{k}}};\quad \eta_{k-1,2} = \frac{\left|\overrightarrow{J\bar{k}}\right|}{h_{Jk}^{\hat{k-1}}} \tag{A.9}$$

and:

$$T_{\hat{k},1}^{(n)} = \lambda_{\bar{k}\overline{k-1}} \frac{\left(\vec{N}_{J\bar{k}}\right)^T \underset{\sim}{K}_{\hat{k}} \left(\vec{N}_{J\bar{k}}\right)}{\left|\overrightarrow{J\bar{k}}\right|^2}; \quad T_{\hat{k},2}^{(n)} = \lambda_{\bar{k}\overline{k+1}} \frac{\left(\vec{N}_{J\overline{k+1}}\right)^T \underset{\sim}{K}_{\hat{k}} \left(\vec{N}_{J\overline{k+1}}\right)}{\left|\overrightarrow{J\overline{k+1}}\right|^2};$$

$$T_{\hat{k},1}^{(t)} = \lambda_{\bar{k}\overline{k-1}} \frac{\left(\vec{N}_{J\bar{k}}\right)^T \underset{\sim}{K}_{\hat{k}} \left(\overrightarrow{J\bar{k}}\right)}{\left|\overrightarrow{J\bar{k}}\right|^2}; \; T_{\hat{k},2}^{(t)} = \lambda_{\bar{k}\overline{k+1}} \frac{\left(\vec{N}_{J\overline{k+1}}\right)^T \underset{\sim}{K}_{\hat{k}} \left(\overrightarrow{J\overline{k+1}}\right)}{\left|\overrightarrow{J\overline{k+1}}\right|^2}; \tag{A.10}$$

Rewriting the Equation (A.8), the following expression is obtained:

$$\frac{T_{\hat{k},1}^{(n)} \eta_{k,1} \left(p_{\hat{k}} - p_J\right) + T_{\hat{k-1},2}^{(n)} \eta_{k-1,2} \left(p_{\hat{k-1}} - p_J\right)}{T_{\hat{k},1}^{(t)} + T_{\hat{k},1}^{(n)} \cot\theta_{\hat{k},1} - T_{\hat{k-1},2}^{(t)} + T_{\hat{k-1},2}^{(n)} \cot\theta_{\hat{k-1},2}} = \left(p_{\bar{k}} - p_J\right) \tag{A.11}$$

Analogously:

$$\frac{T_{\hat{k+1},1}^{(n)} \eta_{k+1,1} \left(p_{\hat{k+1}} - p_J\right) + T_{\hat{k},2}^{(n)} \eta_{k,2} \left(p_{\hat{k}} - p_J\right)}{T_{\hat{k+1},1}^{(t)} + T_{\hat{k+1},1}^{(n)} \cot\theta_{\hat{k+1},1} - T_{\hat{k},2}^{(t)} + T_{\hat{k},2}^{(n)} \cot\theta_{\hat{k},2}} = \left(p_{\overline{k+1}} - p_J\right) \tag{A.12}$$

Then, substituting (A.11) in (A.6), the following expression is obtained:

$$\sum_{k=1}^{n_J} \xi_k \left[T_{\hat{k},1}^{(n)} \eta_{k,1} \left(p_{\hat{k}} - p_J\right) + T_{\hat{k-1},2}^{(n)} \eta_{k-1,2} \left(p_{\hat{k-1}} - p_J\right) \right] = 0 \tag{A.13}$$

where:

$$\xi_k = \frac{\overline{T}_{\hat{k-1}}^{(t)} - \overline{T}_{\hat{k}}^{(t)} + \overline{T}_{\hat{k-1}}^{(n)} \cot\vartheta_{\hat{k-1},1} + \overline{T}_{\hat{k}}^{(n)} \cot\vartheta_{\hat{k},2}}{T_{\hat{k-1},2}^{(n)} \cot\theta_{\hat{k-1},2} + T_{\hat{k},1}^{(n)} \cot\theta_{\hat{k},1} - T_{\hat{k-1},2}^{(t)} + T_{\hat{k},1}^{(t)}} \tag{A.14}$$

As indicated in Equation (A.12), each term $\left(p_{\hat{k}} - p_J\right)$ will appear in two auxiliary variables expressions, so the Equation (A.13) can be rewritten in the following generalizing form:

$$\sum_{k=1}^{n_J} \left(\xi_k T_{\hat{k},1}^{(n)} \eta_{k,1} + \xi_{k+1} T_{\hat{k},2}^{(n)} \eta_{k,2} \right) \left(p_{\hat{k}} - p_J\right) = 0 \tag{A.15}$$

Then:

$$\frac{\sum_{k=1}^{n_J} \left(\xi_k T_{\hat{k},1}^{(n)} \eta_{k,1} + \xi_{k+1} T_{\hat{k},2}^{(n)} \eta_{k,2} \right) p_{\hat{k}}}{\sum_{k=1}^{n_J} \left(\xi_k T_{\hat{k},1}^{(n)} \eta_{k,1} + \xi_{k+1} T_{\hat{k},2}^{(n)} \eta_{k,2} \right)} = p_J \tag{A.16}$$

Or alternatively:

$$p_J = \sum_{k=1}^{n_J} \frac{\xi_k T_{\hat{k},1}^{(n)} \eta_{k,1} + \xi_{k+1} T_{\hat{k},2}^{(n)} \eta_{k,2}}{\sum_{k=1}^{n_J} \left(\xi_k T_{\hat{k},1}^{(n)} \eta_{k,1} + \xi_{k+1} T_{\hat{k},2}^{(n)} \eta_{k,2} \right)} p_{\hat{k}} = \sum_{k=1}^{n_J} \frac{\lambda_{\hat{k}}}{\sum_{k=1}^{n_J} \lambda_{\hat{k}}} p_{\hat{k}} = \sum_{k=1}^{n_J} w_{\hat{k}} p_{\hat{k}} \tag{A.17}$$

If the node to be interpolated is on the boundary, the flux crossing the boundary edges need to be considered, then the Equation (A.6) becomes:

$$\sum_{k=1}^{n_J} \left(\overline{T}_{\hat{k}}^{(t)} - \overline{T}_{\hat{k}}^{(n)} \cot \vartheta_{\hat{k},2} \right) \left(p_{\overline{k}} - p_J \right) - \left(\overline{T}_{\hat{k}}^{(t)} + \overline{T}_{\hat{k}}^{(n)} \cot \vartheta_{\hat{k},1} \right) \left(p_{\overline{k+1}} - p_J \right) + F_1 + F_{n_J+1} = 0 \tag{A.18}$$

where $F_1 + F_{n_J+1}$ is the total flow crossing the boundary edges. The continuity imposing on the boundary edges need to be done as following:

$$\begin{cases} \vec{v}_{J\overline{1}} \cdot \vec{N}_{J\overline{1}} + F_1 = 0 \\ \vec{v}_{\overline{n_J+1}J} \cdot \vec{N}_{\overline{n_J+1}J} + F_{n_J+1} = 0 \end{cases} \tag{A.19}$$

It leads, through Lemma 1, to:

$$\begin{cases} \dfrac{T_{\hat{1},1}^{(n)} \eta_{1,1} \left(p_{\hat{1}} - p_J \right) - F_1}{T_{\hat{1},1}^{(t)} + T_{\hat{1},1}^{(n)} \cot \theta_{\hat{1},1}} = \left(p_{\overline{1}} - p_J \right) \\ \dfrac{T_{\hat{n}_J,2}^{(n)} \eta_{n_J,2} \left(p_{\hat{n}_J} - p_J \right) - F_{n_J+1}}{T_{\hat{n}_J,2}^{(n)} \cot \theta_{\hat{n}_J,2} - T_{\hat{n}_J,2}^{(t)}} = \left(p_{\overline{n}_J} - p_J \right) \end{cases} \tag{A.20}$$

Substituting (A.11) and (A.20) in (A.18), the following expression is obtained:

$$p_J = \frac{1}{\sum_{k=1}^{n_J} \lambda_{\hat{k}}} \left[\sum_{k=1}^{n_J} \lambda_{\hat{k}} p_{\hat{k}} - \sum_{k=1;n_J+1} \left(1 + \xi_k \right) F_k \right] \tag{A.21}$$

where:

$$\begin{cases} \xi_1 = \dfrac{\overline{T}_{\hat{1}}^{(n)} \cot \vartheta_{\hat{1},2} - \overline{T}_{\hat{1}}^{(t)}}{T_{\hat{1},1}^{(n)} \cot \theta_{\hat{1},1} + T_{\hat{1},1}^{(t)}} \\ \xi_{n_J+1} = \dfrac{\overline{T}_{n_J \hat{+}1}^{(n)} \cot \vartheta_{n_J \hat{+}1,1} + \overline{T}_{n_J \hat{+}1}^{(t)}}{T_{n_J \hat{+}1,2}^{(n)} \cot \theta_{n_J \hat{+}1,2} - T_{n_J \hat{+}1,2}^{(t)}} \end{cases} \tag{A.22}$$